

**Chapter 4. A Tetrahedrally Coordinated  $L_3Fe-N_x$  Platform that  
Accommodates Terminal Nitride ( $Fe^{IV}\equiv N$ ) and Dinitrogen ( $Fe^I-N_2-Fe^I$ )  
Ligands**

*The text of this chapter is reproduced in part with permission from:*

Betley, T. A.; Peters, J. C. *J. Am. Chem. Soc.* **2004**, *126*, 6252.

*Copyright 2004 American Chemical Society.*

**Abstract**

A tetrahedrally coordinated  $L_3Fe-N_x$  platform that accommodates both terminal nitride ( $L_3Fe^{IV}\equiv N$ ) and dinitrogen ( $L_3Fe^I-N_2-Fe^IL_3$ ) functionalities is described. The diamagnetic  $L_3Fe^{IV}\equiv N$  species featured has been characterized in solution under ambient conditions by multinuclear NMR ( $^1H$ ,  $^{31}P$ , and  $^{15}N$ ) and infrared spectroscopy. The electronic structure of the title complex has also been explored using DFT. The terminal nitride complex oxidatively couples to generate the previously reported  $L_3Fe^I-N_2-Fe^IL_3$  species. This reaction constitutes a six-electron transformation mediated by two iron centers. Reductive protonation of the nitride complex releases  $NH_3$  as a significant reaction product.

## 4.1 Introduction

High-oxidation state iron complexes featuring metal-to-ligand multiple bonds (e.g., Fe=E/Fe≡E) are proposed as key intermediates in numerous biocatalytic transformations.<sup>1</sup> Because such intermediates are typically too reactive to be directly observed,<sup>2a</sup> much effort has focused on developing low-molecular weight model complexes that enable the more systematic study of their physical characteristics and reactivity patterns.<sup>1,2b</sup> The vast majority of work in this field has been devoted to reactive ferryls (Fe<sup>IV</sup>=O) as these species are postulated as critical intermediates in a variety of enzymes that reduce dioxygen.<sup>3</sup> The reduction of dinitrogen constitutes an equally fascinating biocatalytic transformation.<sup>4</sup> A highly redox-active molybdenum center (Mo<sup>III</sup> to Mo<sup>VI</sup>) has been suggested as the site of N<sub>2</sub> binding and reduction in the well-studied FeMo cofactor.<sup>5</sup> Schrock's demonstration of catalytic ammonia production using a well-defined tris(amido)amine molybdenum complex elegantly establishes that such a scenario is chemically feasible.<sup>6</sup> One of the various alternative possibilities to consider is that a single low-valent iron site<sup>5a,7</sup> initiates the required redox transformations to convert N<sub>2</sub> to NH<sub>3</sub> by successive H<sup>+</sup>/e<sup>-</sup> transfer steps (e.g., Fe<sup>I</sup>-N<sub>2</sub> + 3 H<sup>+</sup> + 3 e<sup>-</sup> → Fe<sup>IV</sup>≡N + NH<sub>3</sub>; Fe<sup>IV</sup>≡N + 3 H<sup>+</sup> + 3 e<sup>-</sup> → Fe<sup>I</sup>-NH<sub>3</sub>).

An intriguing intermediate to consider under the latter scenario is the iron nitride (Fe≡N). At present, the only spectroscopic evidence for terminally bound nitrides of iron comes from frozen matrix experiments.<sup>8</sup> Nakamoto and co-workers reported the resonance Raman detection of an octaethylporphyrinato nitride (OEP)Fe<sup>V</sup>(N) formed via photochemically induced N<sub>2</sub> expulsion from a coordinated azide ligand.<sup>8a</sup> Wieghardt and

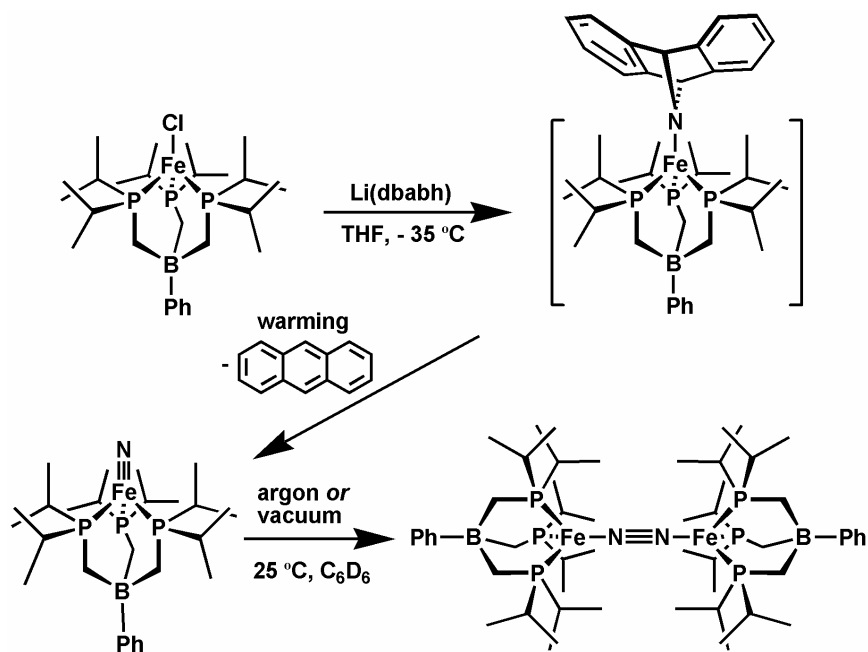
co-workers used a similar photochemical strategy to generate a high-valent iron species assigned as an  $\text{Fe}^{\text{V}}(\text{N})$  nitride based upon low-temperature EPR and Mossbauer data.<sup>8b</sup> The conditions under which these  $\text{Fe}^{\text{V}}(\text{N})$  species were produced, in addition to their high degree of thermal instability, vitiated their more thorough spectroscopic and chemical interrogation. Herein we report the room-temperature observation of what is, to our knowledge, the first terminal iron(IV) nitride,  $[\text{PhBP}^{i\text{Pr}}_3]\text{Fe}^{\text{IV}}\equiv\text{N}$  (**4.1**,  $[\text{PhBP}^{i\text{Pr}}_3] = [\text{PhB}(\text{CH}_2\text{P}^i\text{Pr}_2)_3]$ ).<sup>9</sup> The pseudotetrahedral  $\text{L}_3\text{Fe}-\text{N}_x$  platform described shuttles between the formal oxidation states  $\text{Fe}^{\text{IV}}$  and  $\text{Fe}^{\text{I}}$  as the terminal  $\text{N}_x$  ligand is transformed from the nitride functionality ( $\text{Fe}^{\text{IV}}\equiv\text{N}$ ) to dinitrogen ( $\text{Fe}^{\text{I}}-\text{N}_2-\text{Fe}^{\text{I}}$ ). In addition, the  $\text{Fe}^{\text{IV}}\equiv\text{N}$  subunit can serve as a source of  $\text{NH}_3$  in the presence of proton and electron equivalents.

#### 4.2 Synthesis: Results and Discussion

To explore the viability of a pseudotetrahedral iron nitride  $\text{L}_3\text{Fe}^{\text{IV}}\equiv\text{N}$ , we sought an anionic X-type ligand that would undergo clean oxidative N-atom transfer once coordinated to the "[ $\text{PhBP}^{i\text{Pr}}_3$ ] $\text{Fe}$ " template. Choice of the "[ $\text{PhBP}^{i\text{Pr}}_3$ ] $\text{Fe}$ " subunit as a suitable N-atom acceptor stemmed from prior work by our lab concerning the preparation of pseudotetrahedral, *low-spin*  $S = 1/2$  Fe(III) imides of the type  $[\text{PhB}(\text{CH}_2\text{PPh}_2)_3]\text{Fe}\equiv\text{NR}$  and  $[\text{PhBP}^{i\text{Pr}}_3]\text{Fe}\equiv\text{NR}$ .<sup>7c,10</sup> The lithium amide reagent  $\text{Li}(\text{dbabh})$  ( $\text{dbabh} = 2,3:5,6$ -dibenzo-7-aza bicyclo[2.2.1]hepta-2,5-diene),<sup>11</sup> which has been previously used by Cummins as an N-atom transfer agent,<sup>11b</sup> provided clean access to the desired reaction manifold (Scheme 4.1). Addition of  $\text{Li}(\text{dbabh})$  to yellow  $[\text{PhBP}^{i\text{Pr}}_3]\text{FeCl}$  (**2.2**) in THF (or THF- $d_8$ ) at ca.  $-100$  °C formed a slurry which, upon warming to  $-35$  °C, generated a red species that is formulated as the high-spin amide complex  $[\text{PhBP}^{i\text{Pr}}_3]\text{Fe}(\text{dbabh})$  (**4.2**). For comparison, a structurally related and thermally stable red iron amide complex,

$[\text{PhBP}^{i\text{Pr}}_3]\text{Fe}(\text{NPh}_2)$  (**4.3**), has been isolated and structurally characterized (see Experimental Section 4.5 for details). The reaction between  $\text{Li}(\text{dbabh})$  and chloride **2.2** to generate  $[\text{PhBP}^{i\text{Pr}}_3]\text{Fe}(\text{dbabh})$  can be monitored *in situ* by NMR spectroscopy in  $\text{THF-}d_8$  and proceeds cleanly. A broad optical band associated with amide **4.2** is observed at 475 nm ( $\epsilon = 2300 \text{ M}^{-1} \text{ cm}^{-1}$ ), well-separated from yellow **2.2** (420 nm) and  $\text{Li}(\text{dbabh})$  (370 nm).

*Scheme 4.1*



$[\text{PhBP}^{i\text{Pr}}_3]\text{Fe}(\text{dbabh})$  is thermally unstable and exhibits clean first-order decay when warmed to room temperature in solution ( $t_{1/2} \approx 11$  min at 22 °C)<sup>12</sup> to produce a stoichiometric equivalent of anthracene (NMR integration) and a new diamagnetic iron species assigned as the terminal nitride complex  $[\text{PhBP}^{i\text{Pr}}_3]\text{Fe}\equiv\text{N}$  (**4.1**) on the basis of its NMR data. The <sup>31</sup>P NMR spectrum of the reaction solution (in THF-*d*<sub>8</sub>) shows a single sharp resonance at 84 ppm (Figure 4.1 inset) that is close in chemical shift to the structurally related complex  $[\text{PhBP}^{i\text{Pr}}_3]\text{Co}\equiv\text{N}$ -*p*-tolyl (85 ppm).<sup>7c</sup> The <sup>1</sup>H NMR resonances for the chelated  $[\text{PhBP}^{i\text{Pr}}_3]$  ligand are also indicative of chemically equivalent phosphine donors (Figure 4.1), even at low temperature (-80 °C). While these NMR data are consistent with a three-fold symmetric, pseudotetrahedral structure type, a <sup>15</sup>N-labeling experiment was critical to more firmly establish the Fe≡N functionality. Terminally bound nitrides give rise to signature resonances by <sup>15</sup>N NMR spectroscopy.<sup>13</sup> The diamagnetic nature of the d<sup>4</sup> **4.1** complex therefore renders it particularly well-suited to direct NMR detection of the terminal nitride ligand of interest. A <sup>15</sup>N-labeled sample of Li(dbabh) was prepared from commercially available <sup>15</sup>N-labeled (ca. 98% <sup>15</sup>N) potassium phthalimide (see Experimental Section). Addition of <sup>15</sup>N-Li(dbabh) to **2.2** at low temperature in THF and subsequent warming of the sample to 22 °C for 25 min produced the expected  $[\text{PhBP}^{i\text{Pr}}_3]\text{Fe}\equiv^{15}\text{N}$  (**4.1**·<sup>15</sup>N) nitride product (<sup>31</sup>P NMR). The sample was then cooled to -5 °C, and a high-quality <sup>15</sup>N NMR spectrum was obtained over a period of 8 h. The <sup>15</sup>N NMR spectrum is shown in Figure 4.2 (top panel) and exhibits a single sharp resonance at 952 ppm (referenced to nitromethane at 380 ppm), cementing our assignment of the complex as cylindrically symmetric with a terminally bound  $\text{Fe}\equiv\text{N}$  linkage.<sup>14</sup>

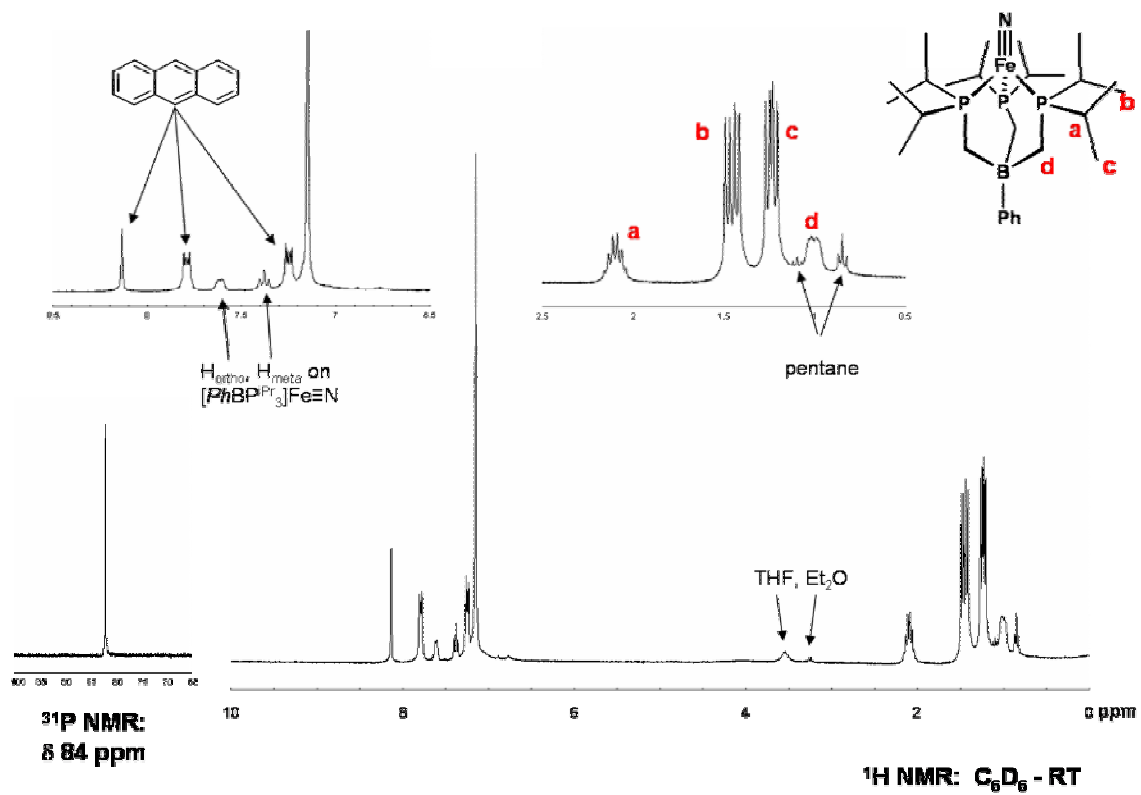


Figure 4.1.  $^1\text{H}$  NMR and  $^{31}\text{P}$  NMR of  $[\text{PhBP}^{i\text{Pr}}_3]\text{Fe}\equiv\text{N}$  (4.1).

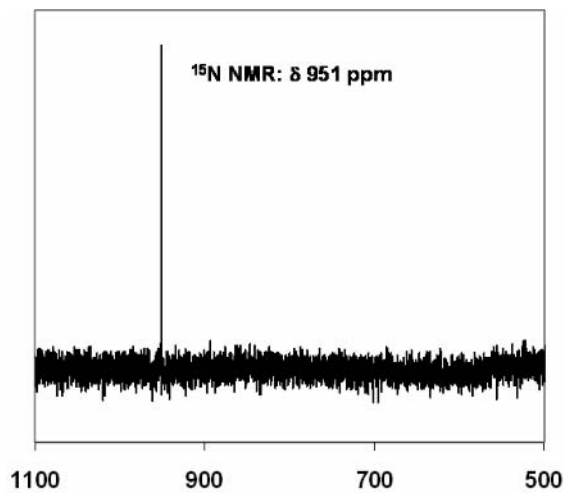
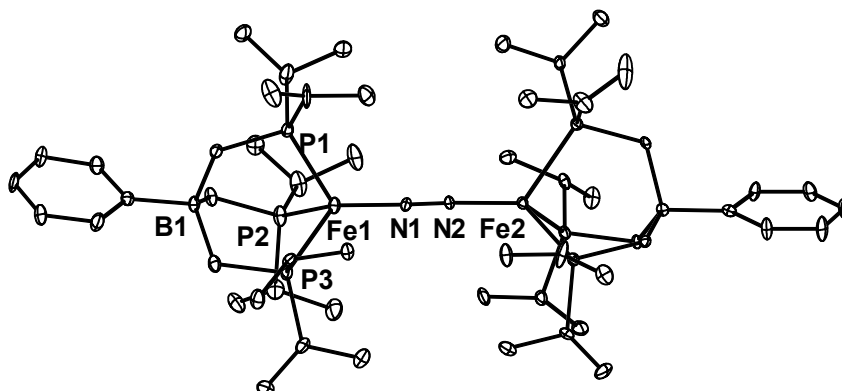


Figure 4.2.  $^{15}\text{N}$  NMR  $[\text{PhBP}^{i\text{Pr}}_3]\text{Fe}\equiv^{15}\text{N}$  (4.1- $^{15}\text{N}$ ).

Akin to several high-valent osmium and ruthenium nitrides,<sup>15</sup> **4.1** exhibits a propensity to undergo bimolecular condensation via nitride coupling (Scheme 4.1). This process generates the previously reported N<sub>2</sub>-bridged complex  $\{[\text{PhBP}^{i\text{Pr}}_3]\text{Fe}\}_2(\mu\text{-N}_2)$  (**3.7**).<sup>7c</sup> The coupling reaction takes place under an argon atmosphere or upon concentration under vacuum. The solid-state molecular structure of **3.7** has been obtained by X-ray diffraction analysis, and its X-ray structural representation is shown in Figure 4.3. The bimolecular coupling reaction of **4.1** is striking in that it constitutes what is, to our knowledge, the only example of a 6-electron redox process mediated by two iron centers. Each iron center formally shuttles from Fe<sup>IV</sup> to Fe<sup>I</sup> as the N<sub>x</sub> ligand is transformed from a  $\pi$ -basic nitride to  $\pi$ -acidic N<sub>2</sub>. While the converse of this pathway (i.e., Fe<sup>I</sup>-N $\equiv$ N-Fe<sup>I</sup>  $\rightarrow$  2 Fe<sup>IV</sup> $\equiv$ N) is therefore kinetically competent by microscopic reversibility, it may not be thermally accessible in the present system. Heating a THF solution of **3.7** at 60 °C brought about its gradual degradation; however, no [PhBP<sup>*i*Pr</sup><sub>3</sub>Fe $\equiv$ N] was detected, and the various reaction products produced were ill-defined. Evidence for a viable Fe<sup>I</sup>-to-Fe<sup>IV</sup> redox couple was demonstrated by the addition of a high-valent Mn<sup>V</sup> $\equiv$ N source,<sup>16</sup> (*trans*-[1,2-cyclohexanediamino-*N,N'*-bis(4-diethylaminosalicylidene)]Mn<sup>V</sup> $\equiv$ N (**4.5**), to the dinitrogen-bridged complex **3.7**. Mixing a stoichiometric equivalent of these two complexes in THF solution generated **4.1** in minutes (~40% based on Fe; Scheme 4.2). The reaction did not proceed to completion, and the reaction mixture likely contained equilibrating species.<sup>17</sup>



**Figure 4.3.** Molecular representation of the solid-state structure of  $\{[\text{PhBP}^{i\text{Pr}}_3]\text{Fe}\}_2(\mu^2\text{-N}_2)$  (**3.7**).  $\text{Fe1-N1} = 1.811(5) \text{ \AA}$ ;  $\text{Fe2-N2} = 1.818(5) \text{ \AA}$ ;  $\text{N1-N2} = 1.138(6) \text{ \AA}$ . See Experimental Section for details.

While the  $\text{Fe}^{\text{IV}}\equiv\text{N}$  coupling reaction to produce  $\text{Fe}^{\text{I}}\text{-N}\equiv\text{N-Fe}^{\text{I}}$  under argon further substantiates our assignment of the terminal nitride functionality, it has also frustrated our efforts to isolate **4.1** in crystalline form. To obtain satisfactory vibrational characterization of the  $\text{Fe}\equiv\text{N}$  functional unit, it was necessary to reconstitute the nitride complex in a straight-chain hydrocarbon. To do this while circumventing its concentration-dependent degradation to **3.7**, a  $\sim 0.02 \text{ M}$  solution of the amide  $[\text{PhBP}^{i\text{Pr}}_3]\text{Fe}(\text{dbabh})$  was generated at  $-35 \text{ }^\circ\text{C}$  in THF and then dried by removal of the reaction volatiles without warming the solution. The remaining residue was reconstituted in cold pentane and subsequently warmed to  $22 \text{ }^\circ\text{C}$  to generate a solution containing **4.1** and the anthracene byproduct (see Experimental Section). Examination of the respective IR spectra of pentane solutions of  $[\text{PhBP}^{i\text{Pr}}_3]\text{Fe}\equiv\text{N}$  and  $[\text{PhBP}^{i\text{Pr}}_3]\text{Fe}\equiv^{15}\text{N}$  prepared in this fashion reveals an  $\nu(\text{Fe}\equiv\text{N})$  vibration at  $1034 \text{ cm}^{-1}$  and an  $\nu(\text{Fe}\equiv^{15}\text{N})$  vibration at  $1007 \text{ cm}^{-1}$ .

<sup>1</sup> (Figure 4.4). The isotopically labeled derivative thus shifts to lower frequency by 27  $\text{cm}^{-1}$ , the amount predicted from the reduced mass calculation for a simple harmonic oscillator model ( $28 \text{ cm}^{-1}$ ). The energy of the  $\text{Fe}\equiv\text{N}$  vibration is reflective of the  $\text{Fe}\equiv\text{N}$  triple bond (vide infra) and is to be compared with related data for other bona fide  $\text{M}\equiv\text{N}$  triple bonds. For example, the  $\text{Mn}\equiv\text{N}$  vibration in  $(\text{TPP})\text{Mn}\equiv\text{N}$  is  $1036 \text{ cm}^{-1}$  ( $^{15}\text{N}$ :  $1008 \text{ cm}^{-1}$ ) and the  $\text{Mo}\equiv\text{N}$  vibration in Schrock's  $[\text{IPTN}_3\text{N}]\text{Mo}\equiv\text{N}$  is  $1013 \text{ cm}^{-1}$  ( $^{15}\text{N}$ :  $986 \text{ cm}^{-1}$ ).<sup>13b,18,19</sup> Nakamoto reported a much lower vibration ( $876 \text{ cm}^{-1}$ ) for an  $(\text{TPP})\text{Fe}^{\text{V}}(\text{N})$  species detected in a frozen glass.<sup>8a</sup> The lower frequency for  $(\text{TPP})\text{Fe}^{\text{V}}(\text{N})$  likely results from attenuation of the  $\text{Fe}-\text{N}$  bond order ( $\text{Fe}=\text{N}$ ) due to occupation of the  $\text{Fe}-\text{N} \pi^*$  orbitals by two electrons.

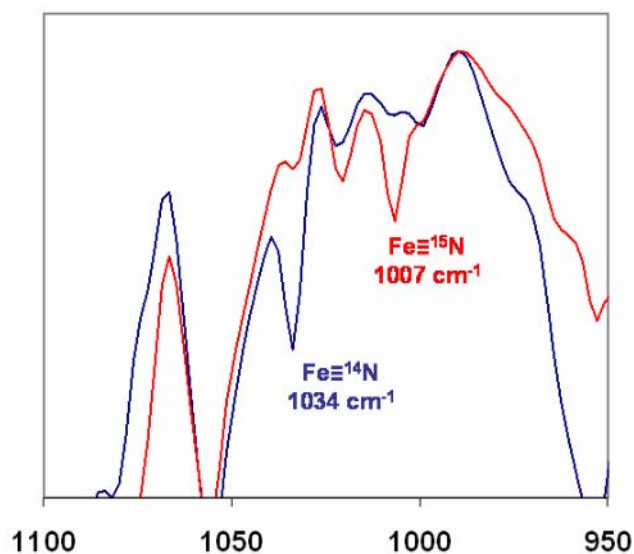


**Figure 4.4.** IR (pentane/KBr): (blue line)  $[\text{PhBP}^{i\text{Pr}}_3]\text{Fe}\equiv^{14}\text{N}$  (**4.1**), (red line)  $[\text{PhBP}^{i\text{Pr}}_3]\text{Fe}\equiv^{15}\text{N}$  (**4.1-<sup>15</sup>N**).

Both five- and even six-coordinate iron complexes can be prepared using the [PhBP<sup>iPr</sup><sub>3</sub>] ligand scaffold,<sup>9</sup> and we therefore suggest that there is an electronic stabilization of the Fe≡N linkage under three-fold symmetry that arises from the possibility to achieve one  $\sigma$ - and two  $\pi$ -bonding interactions. That this should be the case can be easily predicted from simple symmetry considerations and is also supported by DFT calculations. A DFT-minimized geometry for **4.1** has been determined using the atomic coordinates reported previously for the  $S = 1/2$  imide complex [PhBP<sup>iPr</sup><sub>3</sub>]Fe≡NAd as an initial HF guess.<sup>7c,20</sup> The calculation provides the geometric and electronic structure information provided in Figure 4.4. The Fe-N bond distance is calculated at 1.49 Å, appreciably shorter than the distance for its crystallographically characterized relative [PhBP<sup>iPr</sup><sub>3</sub>]Fe≡NAd (**3.11**,  $d_{\text{Fe-N}}$  1.64 Å).<sup>7c</sup> The P-Fe-P angles are appreciably expanded (99-101°) in the calculated nitride structure by comparison to their more typical angles in a host of other [PhBP<sup>iPr</sup><sub>3</sub>]Fe complexes (90-95°),<sup>7c,9</sup> lending it a conformation that is somewhat more tetrahedral in nature. This fact, in addition to the distinct N-atom hybridization in the nitride complex by comparison to related imide structures,<sup>21</sup> dramatically destabilizes the iron-centered  $a_1$  orbital of  $d_{z^2}$  parentage. This situation gives rise to a large HOMO-LUMO gap for **4.1** and a favorable ground-state  $(xy)^2 (x^2 - y^2)^2 (z^2)^0 (xz)^0 (yz)^0$  electronic configuration consistent with a  $d^4$ ,  $S = 0$  Fe<sup>IV</sup>≡N subunit. The diamagnetic  $d^4$  complex (mesityl)<sub>3</sub>Ir<sup>V</sup>≡O presumably owes its stability to similar electronic arguments.<sup>22</sup>

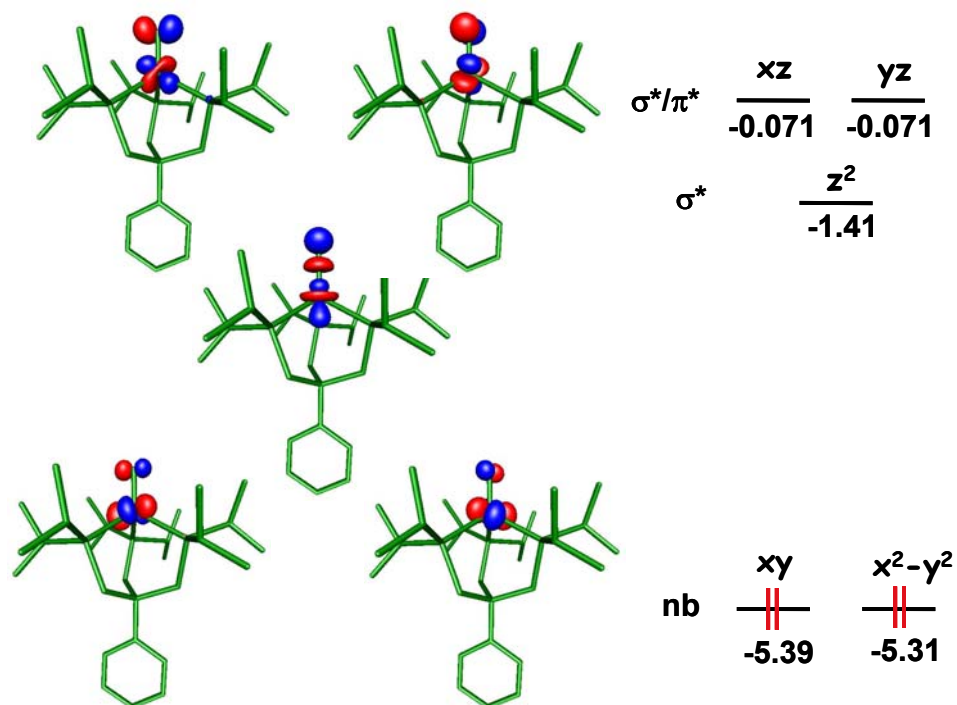


**Figure 4.5.** Theoretically predicted geometry and electronic structure (DFT, JAGUAR 5.0, B3LYP/LACVP\*\*) for  $S = 0$   $[\text{PhBP}^{\text{Pr}}_3]\text{Fe}\equiv\text{N}$  (**4.1**). Lobal representations correspond to the frontier orbitals (energies in eV). Structural parameters: Fe-P = 2.28, 2.28, 2.29 Å; N-P-Fe = 117, 117, 119°; P-Fe-P = 99, 101, 101°; Fe-N = 1.490 Å.

### 4.3 XAS Analysis

Due to the failed attempts to isolate the  $[\text{PhBP}^{i\text{Pr}}_3]\text{Fe}\equiv\text{N}$  in its crystalline form, we sought to gain structural insight into **4.1** via XAS analysis.<sup>23</sup> Three species were submitted for XAS/EXAFS analysis:  $[\text{PhBP}^{i\text{Pr}}_3]\text{Fe}^{\text{IV}}\equiv\text{N}$  (**4.1**),  $[\text{PhBP}^{i\text{Pr}}_3]\text{Fe}^{\text{III}}\equiv\text{NAd}$  (**3.11**), and  $([\text{PhBP}^{i\text{Pr}}_3]\text{Fe}^{\text{I}})_2(\mu^2\text{-N}_2)$  (**3.7**). The latter two species have been structurally characterized crystallographically by X-ray diffraction studies (see Ch. 3 for **3.11** and Figure 4.3 above for **3.7**) and provided a useful benchmark for analysis of the  $\text{Fe}^{\text{IV}}\equiv\text{N}$  framework. While the dinitrogen and imide complexes (**3.7** and **3.11**) were collected as solid matrices diluted with boron nitride (BN) (1:20), the nitride **4.1** was collected as a *d*<sub>8</sub>-toluene solution at a concentration of ca. 30 mM. The preliminary data (Figures 4.6) display the data collected for complexes **3.7**, **3.11**, and **4.1**. The data for **4.1** was complicated by a significant conversion of the nitride to the dinitrogen-bridged dimer **3.7**. Thus, the data represents a ca. 1:1 mixture of the two species whose features are separate and discernable, which can be described.

**4.3.1 XANES.** The pre-edge transitions for complexes **3.7**, **3.11**, and **4.1** are apparent from Figure 4.6 centered around 7113 eV. Nitride **4.1** exhibits an intense  $1s \rightarrow 3d$  pre-edge transition with an area of 50 units (Figure 4.6), whereas the dinitrogen and imide complexes (**3.7** and **3.11**) have pre-edge transition areas more typical of iron complexes (2-8 units for oxidation states  $\text{Fe}^{\text{I}}\text{-Fe}^{\text{III}}$ ). The largest pre-edge transition area previously reported corresponded to the  $\text{Fe}^{\text{IV}}=\text{O}$  oxo species from Que's laboratories.<sup>24</sup> They report pre-edge transitions with areas of up to 30 units for five- and six-coordinate oxo complexes. The unusually large pre-edge transition for **4.1** is attributable to the novel

four-coordinate structure with a high degree of mixing of the 3d and 4p orbitals. Increases in the pre-edge intensity have been correlated with deviations from centrosymmetry. The peak energy of 7113.0 eV is only  $\sim 0.5$  eV higher than the centroid of the peaks for the imide **3.11**. These energies are relatively low for  $\text{Fe}^{\text{III}}$  and  $\text{Fe}^{\text{IV}}$  centers, respectively, and probably arise from the highly covalent character of the Fe–N bonds.

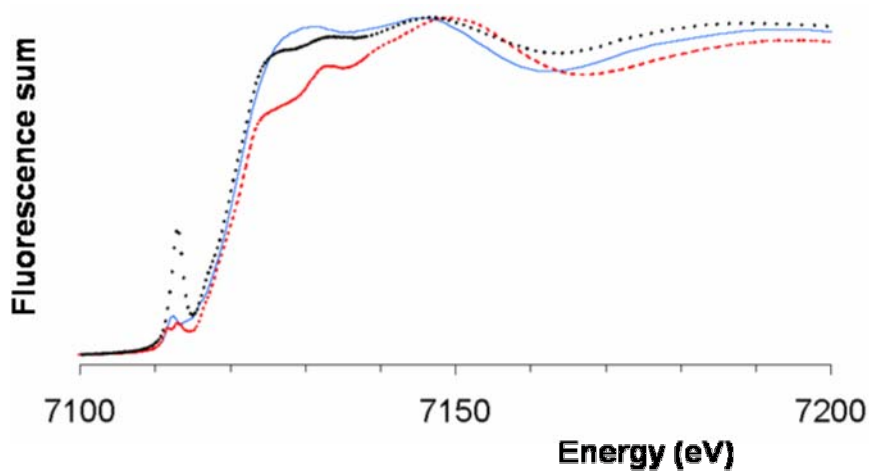


**Figure 4.6.** X-ray absorption near-edge features (Fe K-edge, fluorescence excitation) of **3.7** (solid blue line), **3.11** (dashed red line), **4.1** (dotted black line).

**4.3.2. EXAFS.** The EXAFS data collected for the independently prepared dinitrogen complex **3.7** (Figure 4.7) and the imide complex **3.11** (Figure 4.8) showed excellent agreement with the Fe-N and Fe-P distances determined crystallographically (see Table 4.1 for distance comparisons). The best fit for complex **3.7** shows an O/N feature at 1.79 Å, a P feature with three times the magnitude (proportional to the number of atoms within the coordination sphere) at 2.35 Å, and a feature attributable to an Fe-Fe scattering event at ca. 4.75 Å. The best fit for complex **3.11** shows an O/N feature at 1.64 Å and a P feature with three times the magnitude at 2.27 Å. The  $d^8$ -toluene glass studied for the nitride shows distinct features for a novel Fe-N species and features that match well with an authentically prepared sample for **3.7** (Figure 4.9). The novel Fe-N species shows an O/N feature at 1.54 Å and three P at 2.24 Å. The extremely short Fe-N bond vector is consistent with the terminal Fe≡N assignment, a full 0.1 Å shorter than the structurally characterized Fe<sup>II</sup> imide anions, neutral Fe<sup>III</sup> imides, or Co<sup>III</sup> imides previously reported, more reminiscent of Mn<sup>V</sup>≡N nitride bond lengths (e.g., (salen)Mn<sup>V</sup>≡N,  $d_{\text{Mn-N}}$  1.51 Å).<sup>31</sup> The Fe-P feature at 2.24 Å is fully consistent with the M-P bond lengths for structurally characterized singlet Fe<sup>II</sup> imide anions and (M-P<sub>av</sub> = 2.15 Å) Co<sup>III</sup> imide complexes (M-P<sub>av</sub> = 2.19 Å).

**Table 4.1** Bond distances from EXAFS and X-ray crystallography (in *italics*)

<b>Complex</b>		<b>N/O</b>	<b>P</b>	<b>Fe</b>
<b>3.7</b>	Fe <sub>2</sub> (N <sub>2</sub> )	1.79	2.35	4.75
		<i>1.82</i>	<i>2.36</i>	<i>4.76</i>
<b>3.11</b>	Fe≡NAd	1.64	2.27	--
		<i>1.64</i>	<i>2.27</i>	--
<b>4.1</b>	Fe≡N	1.54	2.24	--
		<i>1.49<sup>a</sup></i>	<i>2.22<sup>a</sup></i>	--
	Fe <sub>2</sub> (N <sub>2</sub> ) <sup>b</sup>	1.82 <sup>b</sup>	2.43 <sup>b</sup>	4.75 <sup>b</sup>

<sup>(a)</sup> From DFT estimations (vida supra). <sup>(b)</sup> Observed as decomposition from **4.1** in *d*<sup>8</sup>-toluene solution.

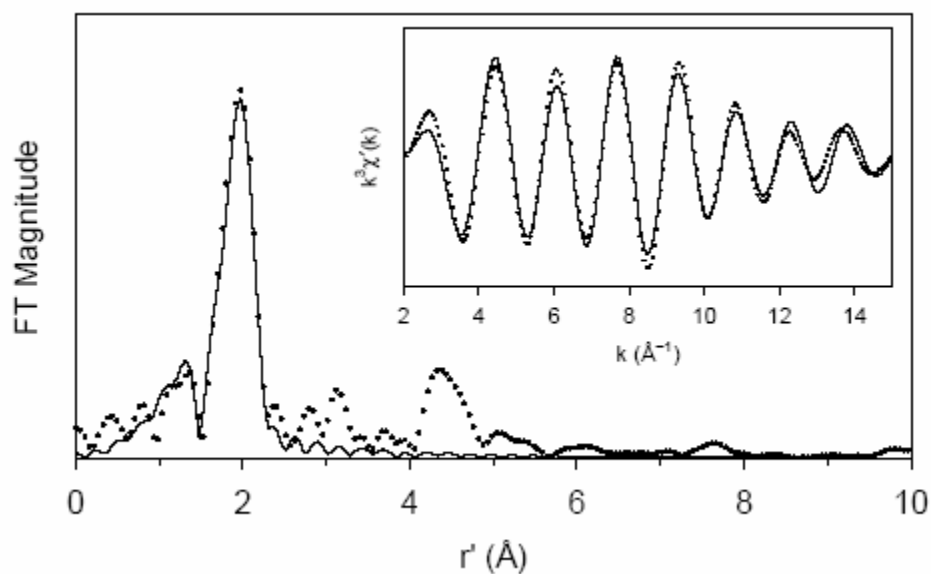


**Figure 4.7.** Fourier transform of the Fe K-edge EXAFS data ( $k^3\chi(k)$ ) and Fourier-filtered EXAFS spectrum ( $k^3\chi'(k)$ , inset) of 30 mM ( $[\text{PhBP}^{i\text{Pr}}_3\text{Fe}]_2(\mu^2\text{-N}_2)$  (**3.7**) in BN (1:20) at  $T = 13$  K, obtained by fluorescence detection. Fourier-transformed range  $k = 2\text{--}15 \text{ \AA}^{-1}$ ; experimental data ( $\bullet\bullet$ ) and best fit ( $\text{—}$ ); fitting: one O/N at 1.79  $\text{\AA}$ , three P at 2.35  $\text{\AA}$ , and one Fe-Fe at 4.75  $\text{\AA}$ . Back-transformation range:  $r' = 0.60\text{--}2.65 \text{ \AA}$ .

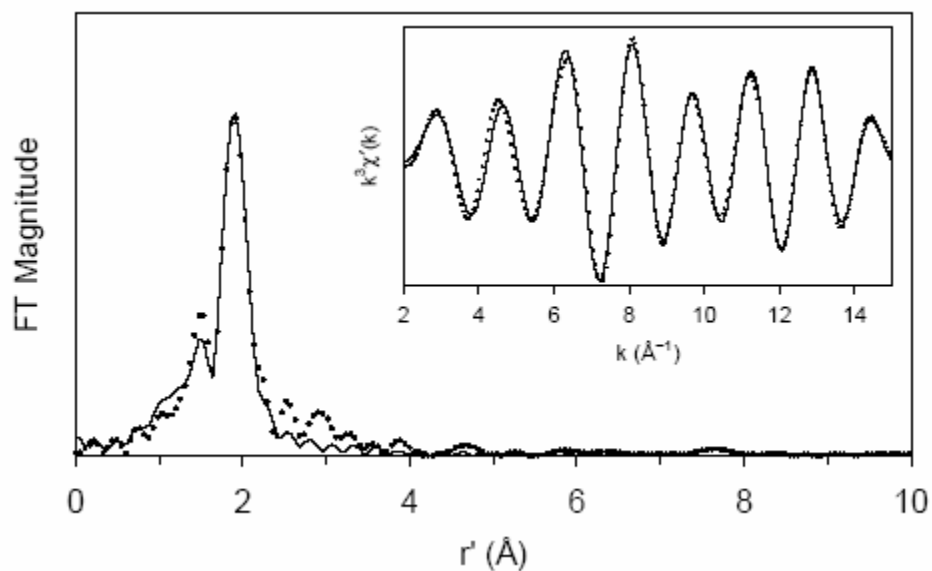


**Figure 4.8.** Fourier transform of the Fe K-edge EXAFS data ( $k^3\chi(k)$ ) and Fourier-filtered EXAFS spectrum ( $k^3\chi'(k)$ , inset) of  $[\text{PhBP}^{i\text{Pr}}_3]\text{Fe}\equiv\text{NAd}$  (**3.11**), Fourier-transformed range  $k = 2\text{--}15 \text{ \AA}^{-1}$ ; experimental data ( $\bullet\bullet\bullet$ ) and fit 1 N, 3 P (—); Back-transformation range:  $r' = 0.65\text{--}2.70 \text{ \AA}$ .

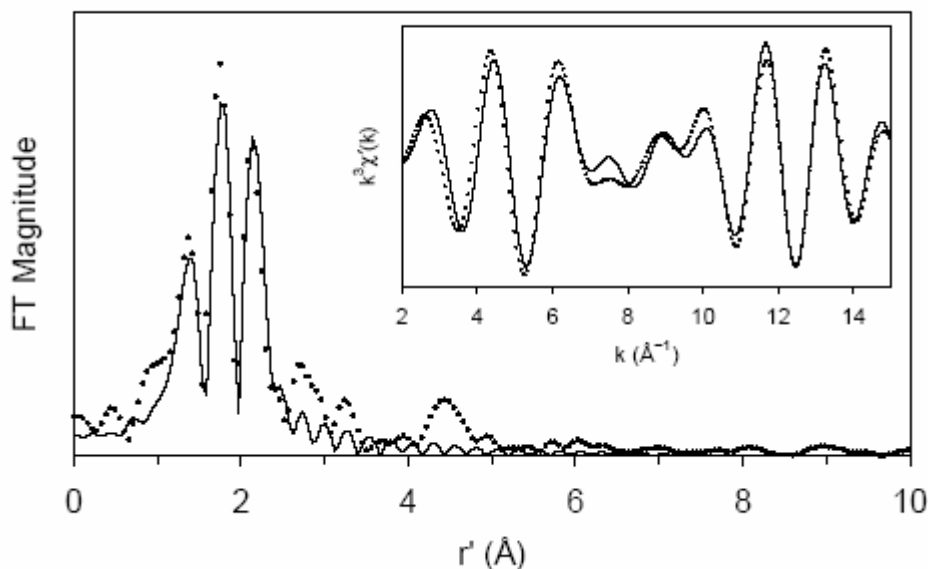


**Figure 4.9.** Fourier transform of the Fe K-edge EXAFS data ( $k^3\chi(k)$ ) and Fourier-filtered EXAFS spectrum ( $k^3\chi'(k)$ , inset) of  $[\text{PhBP}^{i\text{Pr}}_3]\text{Fe}\equiv\text{N}$  (**4.1**) and  $[\text{PhBP}^{i\text{Pr}}_3\text{Fe}]_2(\mu^2\text{-N}_2)$  (**3.7**), Fourier-transformed range  $k = 2\text{--}15 \text{ \AA}^{-1}$ ; experimental data ( $\bullet\bullet$ ) and fit 0.5 N, 0.5 N, 1.5 P, 1.5 P (—); Back-transformation range:  $r' = 0.60\text{--}2.60 \text{ \AA}$ .

#### 4.4 Reactivity

While we have yet to thoroughly survey the reactivity of  $[\text{PhBP}^{i\text{Pr}}_3]\text{Fe}\equiv\text{N}$ , we note the following preliminary observations. The addition of  $\text{PPh}_3$  or  $\text{PEt}_3$  to THF solutions of  $[\text{PhBP}^{i\text{Pr}}_3]\text{Fe}\equiv\text{N}$  appears to cleanly ( $^1\text{H}$  NMR) generate the corresponding  $S = 2$  Fe(II) phosphiniminatos  $[\text{PhBP}^{i\text{Pr}}_3]\text{Fe-N}=\text{PR}_3$  ( $\text{R} = \text{PPh}_3$  or  $\text{PEt}_3$ ). The presence of the phosphiniminato functionality is in each case confirmed by the presence of intense IR vibrations ( $\text{KBr}/\text{C}_6\text{H}_6$ ,  $\nu(\text{Ph}_3\text{P}=\text{N}) = 1223 \text{ cm}^{-1}$ ,  $\nu(\text{Et}_3\text{P}=\text{N}) = 1214 \text{ cm}^{-1}$ ). Also, the corresponding  $\text{R}_3\text{P}=\text{NH}_2^+$  protonolysis products are liberated and detected by subjecting the reaction solutions to positive mode ES-MS (electrospray:  $\text{Ph}_3\text{PNH}_2^+ = m/z 278$ ,

Et<sub>3</sub>PNH<sub>2</sub><sup>+</sup> = *m/z* 120). Perhaps most interesting to note is that the nitride ligand serves as a source of NH<sub>3</sub> upon the addition of proton and electron equivalents. For example, the addition of solid [LutH][BPh<sub>4</sub>] and CoCp<sub>2</sub> (3 equiv of each) to a room-temperature C<sub>6</sub>D<sub>6</sub> solution of [PhBP<sup>*i*Pr</sup><sub>3</sub>]Fe≡N produced after 2 h an appreciable quantity of NH<sub>3</sub>, easily identified by <sup>1</sup>H NMR in *d*<sub>6</sub>-DMSO as its NH<sub>4</sub>Cl salt after vacuum transfer of the reaction volatiles into an ethereal solution of HCl (ca. 1 M).<sup>13b</sup> Two independent runs using these non-optimized conditions afforded 41 and 45% of NH<sub>3</sub> based upon NMR integration versus an internal standard. In a potentially related reaction, the release of *p*-toluidine by hydrogenation of the iron(III) imide [PhB(CH<sub>2</sub>PPh<sub>2</sub>)<sub>3</sub>]Fe≡N-*p*-tolyl was observed.<sup>25</sup>

#### 4.5 Conclusions

To conclude, the "[PhBP<sup>*i*Pr</sup><sub>3</sub>]Fe-N<sub>*x*</sub>" chemistry discussed herein and that which we have reported previously<sup>7c</sup> collectively illustrate that the redox chemistry available to a pseudotetrahedral iron site can be remarkably rich. Examples of "[PhBP<sup>*i*Pr</sup><sub>3</sub>]Fe-N<sub>*x*</sub>" complexes have now been characterized that feature five formal iron oxidation states based upon the magnetic data available:<sup>26</sup> [PhBP<sup>*i*Pr</sup><sub>3</sub>]Fe<sup>0</sup>N<sub>2</sub><sup>-</sup> (*S* = 1), [PhBP<sup>*i*Pr</sup><sub>3</sub>]Fe<sup>I</sup>-N<sub>2</sub>-Fe<sup>I</sup>[PhBP<sup>*i*Pr</sup><sub>3</sub>] (*S* = 3/2 per iron center), [PhBP<sup>*i*Pr</sup><sub>3</sub>]Fe<sup>II</sup>-N<sub>2</sub>Me (*S* = 2), [PhBP<sup>*i*Pr</sup><sub>3</sub>]Fe<sup>III</sup>≡NAd (*S* = 1/2), and [PhBP<sup>*i*Pr</sup><sub>3</sub>]Fe<sup>IV</sup>≡N (*S* = 0). For each of these complexes, the dominant structural modification pertains to the nature of the fourth N<sub>*x*</sub> ligand: π-acidic N<sub>2</sub> favors the lower oxidation states, whereas π-basic nitride (or imide) favors the higher oxidation states.

## 4.6. Experimental Section

**4.6.1 General Considerations.** All manipulations were carried out using standard Schlenk or glove-box techniques under a dinitrogen atmosphere or argon atmosphere when indicated. Unless otherwise noted, solvents were deoxygenated and dried by thorough sparging with N<sub>2</sub> gas followed by passage through an activated alumina column. Non-halogenated solvents were typically tested with a standard purple solution of sodium benzophenone ketyl in tetrahydrofuran in order to confirm effective oxygen and moisture removal. Deuterated solvents were degassed and stored over activated 3-Å molecular sieves prior to use. THF-*d*<sub>8</sub> was dried by passage over activated alumina and stored over activated sieves prior to use. [PhBP<sup>*i*Pr</sup><sub>3</sub>]FeCl,<sup>27</sup> Hdbabh (dbabh = 2,3:5,6-dibenzo-7-aza bicyclo[2.2.1]hepta-2,5-diene),<sup>28</sup> and Li(dbabh)<sup>29</sup> were prepared as previously reported. All reagents were purchased from commercial vendors and used without further purification unless explicitly stated. Elemental analyses were carried out at Desert Analytics, Tucson, Arizona. NMR spectra were recorded at ambient temperature on Varian Mercury 300 MHz, Joel 400 MHz, and an Inova 500 MHz spectrometers, unless otherwise noted. <sup>1</sup>H NMR chemical shifts were referenced to residual solvent. <sup>31</sup>P NMR and <sup>15</sup>N NMR chemical shifts are reported relative to an external standard of 85% H<sub>3</sub>PO<sub>4</sub> (0 ppm) and CH<sub>3</sub>NO<sub>2</sub> (380 ppm relative to liquid ammonia at 0 ppm). GC-MS data was obtained by injecting a dichloromethane solution into a Agilent 6890 GC equipped with an Agilent 5973 mass selective detector (EI). IR spectra were recorded on a Bio-Rad Excalibur FTS 3000 spectrometer controlled by Win-IR Pro software. UV-vis measurements were taken on a Hewlett Packard 8452A diode array spectrometer using a quartz crystal cell with a Teflon cap. X-ray diffraction studies

were carried out in the Beckman Institute Crystallographic Facility on a Bruker Smart 1000 CCD diffractometer.

**4.6.2. X-ray Crystallography Procedures.** X-ray quality crystals were grown as indicated in the experimental procedures for each complex. The crystals were mounted on a glass fiber with Paratone-N oil. Structures were determined using direct methods with standard Fourier techniques using the Bruker AXS software package. In some cases, Patterson maps were used in place of the direct methods procedure to generate initial solutions.

**4.6.3. X-ray absorption spectroscopy (XAS).** XAS data were collected at beamline 9-3 of the Stanford Synchrotron Radiation Laboratory at the Stanford Linear Accelerator, Menlo Park, CA. X-ray absorption spectra at the iron K-edge were collected between 6.9 and 8.0 keV, and the monochromator was calibrated by using the edge energy of iron foil at 7112.0 eV. The data were obtained in fluorescence mode [ $A_{exp}(C_T/C_O)$ ] at 13(1) K. The XAS data analysis protocol has been described.<sup>30</sup>

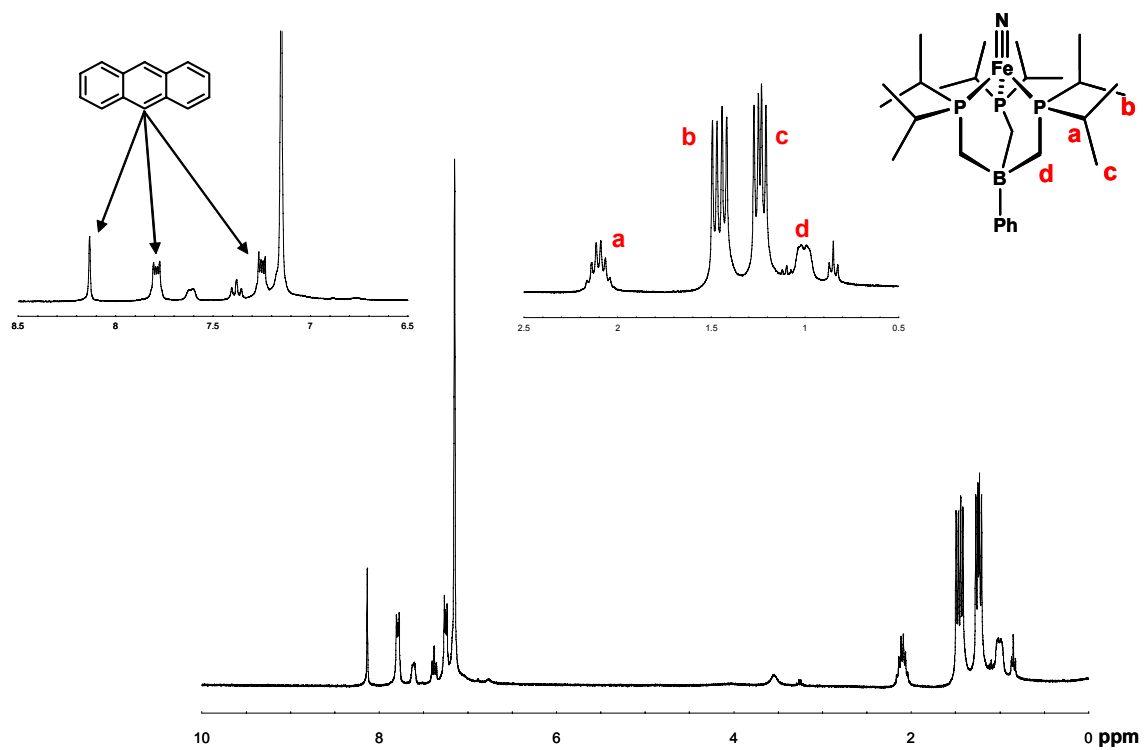
#### **4.6.4. Syntheses of Compounds.**

**<sup>15</sup>N-Hdbabh:** <sup>15</sup>N-potassium phthalimide (98%, Aldrich) (5g, 26.8 mmol) was added to a solution of benzylbromide (4.86 g, 28.4 mmol) in DMF (35 mL) in a 250 mL round-bottom flask in air. The solution was heated to 125 °C for 12 h. Upon cooling the solution to room temperature, 200 mL of cold water was added to the reaction vessel which precipitated the benzylated phthalimide as a white solid. The solids were collected

by filtration over a fritted glass funnel and washed with 1.5 L of water. The solids were dried in vacuum over 18 h to yield 6.27 g (98%) of the benzylated phthalimide (GC-MS,  $^1\text{H}$  NMR). The  $^{15}\text{N}$ -Hdbabh was then prepared following the method of Carpino et al.<sup>28</sup> and lithiated according to Mindiola et al.<sup>29</sup>  $^1\text{H}$  NMR ( $\text{C}_6\text{D}_6$ , 300 MHz):  $\delta$  7.04 (m, 4H), 6.76 (m, 4H), 4.88 (d,  $^2J_{\text{N-H}} = 2.7$  Hz, 2H), 2.65 (bs, 1H, N-H).  $^{15}\text{N}$   $\{^1\text{H}\}$  NMR ( $\text{C}_6\text{D}_6$ , 50.6 MHz):  $\delta$  115 ppm. GC-MS (m/z): 194 (M).

**[PhBP<sup>*i*Pr</sup><sub>3</sub>]FeN (4.1):** A thawing solution of [PhBP<sup>*i*Pr</sup><sub>3</sub>]FeCl (60 mg, 0.105 mmol) in THF (0.2 mL) was added to solid Li(dbabh) (20.9 mg, 0.105 mmol) (c.a. -100°C) (\*  $^{15}\text{N}$ -Li(dbabh) was used to generate [PhBP<sup>*i*Pr</sup><sub>3</sub>]Fe $\equiv$  $^{15}\text{N}$ ). The solution was then stirred vigorously as it warmed to room temperature for 15 minutes. The solution color changes from yellow [PhBP<sup>*i*Pr</sup><sub>3</sub>]FeCl to red as the amide is formed (UV-vis for [PhBP<sup>*i*Pr</sup><sub>3</sub>]Fe-dbabh (THF)  $\lambda_{\text{max}}$ , nm ( $\epsilon$ ,  $\text{M}^{-1} \text{cm}^{-1}$ ): 467 (2300)). After 15 minutes, the solution was placed under vacuum and chilled to -35°C. After 6 h, the red oil was triturated with pentane and evaporated to dryness again, maintaining the temperature at -35 °C. Isolation for IR spectrum: When the solids were dry (2 h in vacuum), the solids were suspended in pentane (3 mL) that dissolve as [PhBP<sup>*i*Pr</sup><sub>3</sub>]FeN forms as the solution warmed to room temperature. The pentane solution was filtered through a glass-fiber filter to remove insolubles. IR: (Pentane/KBr)  $\nu_{\text{FeN}} = 1034 \text{ cm}^{-1}$ ;  $\nu_{\text{Fe}^{15}\text{N}} = 1007 \text{ cm}^{-1}$ . Isolation for NMR spectroscopy: When the solids were dry (2 h in vacuum), the red solid was dissolved in  $\text{C}_6\text{D}_6$  (0.7 mL) at room temperature and filtered through glass-fiber filter paper to remove insoluble material. (See Figure 1)  $^1\text{H}$  NMR ( $\text{C}_6\text{D}_6$ , 300 MHz):  $\delta$  8.13 (s, 2H,  $\text{C}_{14}\text{H}_{14}$ ), 7.79 (m, 4H,  $\text{C}_{14}\text{H}_{14}$ ), 7.60 (m, 2H,  $\text{H}_{\text{ortho}}$  BPh), 7.38 (t, 2H,  $\text{H}_{\text{meta}}$  BPh), 7.25 (m, 4H,

$C_{14}H_{14}$ ), ( $H_{para}$  BPh obscured by anthracene), 2.10 (septet, 6H,  $P(CH(CH_3)_2)$ ), 1.45 (dd,  $J = 7.5, 15.6$  Hz, 18H,  $P(CH(CH_3)_2)$ ), 1.24 (dd,  $J = 7.5, 12.3$  Hz, 18H,  $P(CH(CH_3)_2)$ ), 1.00 (m, 6H,  $B(CH_2PR_2)$ ).  $^{31}P \{^1H\}$  NMR ( $C_6D_6$ , 121.4 MHz):  $\delta$  84.  $^{15}N$  NMR experiment:  $[PhBP^{iPr}_3]FeCl$  (30 mg, 0.052 mmol) and solid  $^{15}N-Li(dbabh)$  (10.5 mg, 0.052 mmol) were added to an NMR tube fitted with a Teflon screw-cap with a capillary tube containing  $OP(OMe)_3$  (7.3 mg, 0.052 mmol) in  $d_8$ -toluene for an internal standard. Thawing THF (0.7 mL) was added to the combined solids in the NMR tube at c.a.  $-100$  °C. The slurry was warmed to  $-42$  °C in a dry ice/acetonitrile bath. The NMR tube was then inserted into the VT-NMR instrument which was precooled to  $-45$  °C. The instrument was warmed to  $-15$  °C to facilitate the amide metathesis reaction. After 30 minutes, the  $[PhBP^{iPr}_3]FeCl$  was consumed as ascertained by  $^1H$  NMR and the instrument was warmed to  $22$  °C for 25 minutes. The production of  $[PhBP^{iPr}_3]Fe^{15}N$  (**4.1- $^{15}N$** ) was monitored via  $^{31}P$  NMR and deemed 85% complete after 25 minutes (integrating vs. internal standard). At this time the instrument was cooled to  $-5$  °C and the  $^{15}N$  NMR acquisition was initiated (duration = 8 h).  $^{15}N \{^1H\}$  NMR (THF, 50.751 MHz):  $\delta$  952 ppm.

**Figure 4.6.1.**  $^1\text{H}$  NMR of  $[\text{PhBP}^{i\text{Pr}}_3]\text{FeN}$  in  $\text{C}_6\text{D}_6$  (scale in ppm).

**[PhBP<sup>iPr</sup><sub>3</sub>]FeNPh<sub>2</sub> (4.3):** A thawing solution of [PhBP<sup>iPr</sup><sub>3</sub>]FeCl (40 mg, 0.070 mmol) in THF (0.2 mL) was added to solid Ph<sub>2</sub>NLi (12.3 mg, 0.072 mmol) (c.a. -100°C). The solution was then stirred vigorously as it warmed to room temperature for 45 minutes. The solution color changes from yellow [PhBP<sup>iPr</sup><sub>3</sub>]FeCl to wine-red as the amide is formed (UV-vis for [PhBP<sup>iPr</sup><sub>3</sub>]FeNPh<sub>2</sub> (THF)  $\lambda_{\text{max}}$ , nm ( $\epsilon$ , M<sup>-1</sup> cm<sup>-1</sup>): 450 (1700)). The volatiles were then removed in vacuo to produce red solid. The solids were dissolved in pentane (5 mL) and filtered through glass-fiber filter paper to remove insolubles. Crystals were grown from a pentane solution stored at -35 °C for 3 days. A crystal was selected from the batch and used for an X-ray diffraction study (see Figure 7). The liquor was decanted from the crystals which were dried in vacuo (35.5mg, 72%). <sup>1</sup>H NMR (C<sub>6</sub>D<sub>6</sub>, 300 MHz):  $\delta$  52.99, 42.57, 20.33, 18.75, 6.78, -0.91, -20.57, -33.30, -55.80. Analyzed for C<sub>39</sub>H<sub>63</sub>BFeNP<sub>3</sub> calculated (found): C, 66.39 (66.31); H, 9.00 (8.89); N, 1.99 (1.76).

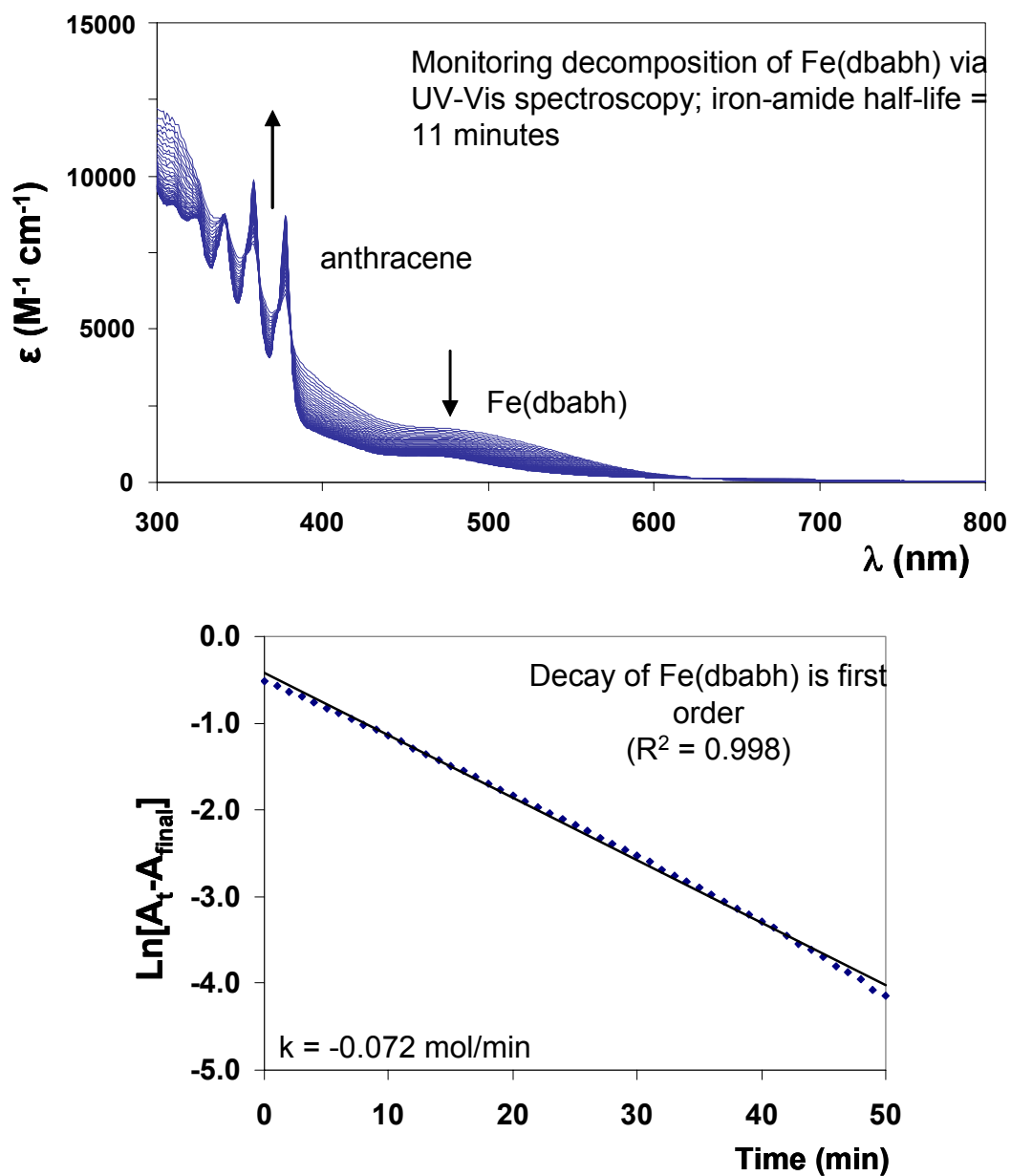
**(Trans-[1,2-cyclohexanediamino-N,N'-bis(4-diethylaminosalicylidene)]Mn<sup>V</sup>≡N (4.5):**  
 The modified salen ligand trans-[1,2-cyclohexanediamino-N,N'-bis(4-diethylaminosalicylidene)] was synthesized by refluxing 4-(diethylamino)salicylaldehyde (2 g, 10.2 mmol) and trans-1,2-diaminocyclohexane (590 mg, 5.2 mmol) in ethanol (150 mL) for 2 h. Cooling the solution to room temperature precipitated the modified salen ligand as yellow crystals. The yellow crystals were collected on a sintered glass frit and dried under vacuum (2 g, 84%). <sup>1</sup>H NMR (C<sub>6</sub>D<sub>6</sub>, 300 MHz):  $\delta$  7.96 (s, 2H), 6.84 (d 2H), 6.37 (d, 2H), 5.91 (dd, 2H), 2.9 (m, 2H), 2.8 (q, 8H), 1.7 (d, 2H), 1.53 (m, 4H), 1.15 (m, 2H), 0.75 (t, 12H). Following the protocol established by Du Bois et al.,<sup>31</sup> the modified

(salen\*)MnN was prepared from the modified salen ligand (2 g, 4.3 mmol), Mn(OAc)<sub>2</sub> (1.108 g, 4.5 mmol), NH<sub>4</sub>OH (4.3 mL, 15 M), and NaOCl (55.5 mL, 0.7 M). The (salen\*)MnN was additionally purified by filtration through a silica plug in 250 mL of CH<sub>2</sub>Cl<sub>2</sub>, followed by removal of solvent and drying in vacuo (1.96 g, 85.7%). <sup>1</sup>H NMR (CD<sub>2</sub>Cl<sub>2</sub>, 300 MHz): δ 7.73 (d, 2H), 7.02 (dd, 2H), 6.14 (m, 2H), 6.12 (s, 2H), 3.37 (q, 8H), 3.32 (m, 2H) 2.91 (m, 1H), 2.51 (dd, 2H), 1.93 (d, 2H), 1.34 (m, 3H), 1.19 (m, 12H). <sup>13</sup>C NMR (CD<sub>2</sub>Cl<sub>2</sub>, 75.459 MHz): 169 (d) 158 (dd), 154, 135 (d), 111 (d), 104 (d), 100 (dd), 99, 72 (dd), 45 (t), 31, 29, 27, 25, 12.5 (q). Analyzed for C<sub>28</sub>H<sub>38</sub>MnN<sub>5</sub>O<sub>2</sub> calculated (found): C, 63.27 (63.02); H, 7.21 (7.55); N, 13.17 (13.11).

**Reaction of {[PhBP<sup>iPr</sup><sub>3</sub>]Fe]<sub>2</sub>(μ-N<sub>2</sub>) with (salen\*)Mn≡N:** A solution of {[PhBP<sup>iPr</sup><sub>3</sub>]Fe]<sub>2</sub>(μ-N<sub>2</sub>) (15 mg, 0.014 mmol) in THF (0.8 mL) was added to solid trans-[1,2-cyclohexanediamino-N,N'-bis(4-diethylaminosalicylidene)]Mn≡N (14.6 mg, 0.028 mmol). The slurry was stirred vigorously for 20 minutes, then transferred to an NMR tube equipped with a capillary tube containing OP(OMe)<sub>3</sub> (7.3 mg, 0.052 mmol) in *d*<sub>8</sub>-toluene for an internal standard. The <sup>31</sup>P {<sup>1</sup>H} NMR shows a peak at 82 ppm that calculates to 41% conversion to [PhBP<sup>iPr</sup><sub>3</sub>]FeN based on iron. <sup>1</sup>H NMR in THF-*d*<sub>8</sub> corroborates this result where yields of [PhBP<sup>iPr</sup><sub>3</sub>]FeN (based on integral standard of Cp<sub>2</sub>Fe) are 37 ± 6% (3 experiments). Reaction of {[PhBP<sup>iPr</sup><sub>3</sub>]Fe]<sub>2</sub>(μ-N<sub>2</sub>) (15 mg, 0.014 mmol) and trans-[1,2-cyclohexanediamino-N,N'-bis(4-diethylaminosalicylidene)]Mn≡N (14.6 mg, 0.028 mmol) in pentane progresses very slowly due to the insolubility of both materials in pentane. The presence of [PhBP<sup>iPr</sup><sub>3</sub>]FeN is discernable in the IR where a peak at (pentane/KBr) ν<sub>FeN</sub> = 1034 cm<sup>-1</sup> is visible.

**4.6.5. UV-Vis kinetics experiment:** A thawing solution of  $[\text{PhBP}^{i\text{Pr}}_3]\text{FeCl}$  (30 mg, 0.052 mmol) in THF (5.0 mL) was added to solid  $\text{Li}(\text{dbabh})$  (10.5 mg, 0.052 mmol) (c.a.  $-100^\circ\text{C}$ ). The 0.01 M solution was then stirred vigorously as it warmed to room temperature for 15 minutes. From this reaction solution, an aliquot of 0.4 mL was diluted to 3.0 mL (THF) in a quartz cuvette (1.3 mM). A full spectrum showing the growth of the anthracene absorptions ( $\lambda = 340, 359, 378 \text{ nm}$ ) and the decay of the band associated with  $[\text{PhBP}^{i\text{Pr}}_3]\text{Fe}(\text{dbabh})$  is shown in Figure 4.6.2. a. The decay of  $[\text{PhBP}^{i\text{Pr}}_3]\text{Fe}(\text{dbabh})$  was monitored by the disappearance of the band at 475 nm over a time period of 65 minutes. No discernable change in the absorption band at 475 nm was discernable after 55 minutes and the reaction was deemed complete. Plotting the  $\text{Ln}(\lambda_{475 \text{ time } t} - \lambda_{475 \text{ final}})$  vs. time (Figure 4.6.2. b) shows that the amide decomposition is 1<sup>st</sup> order (plot is linear) with a half life of 11 minutes at  $22^\circ\text{C}$ .

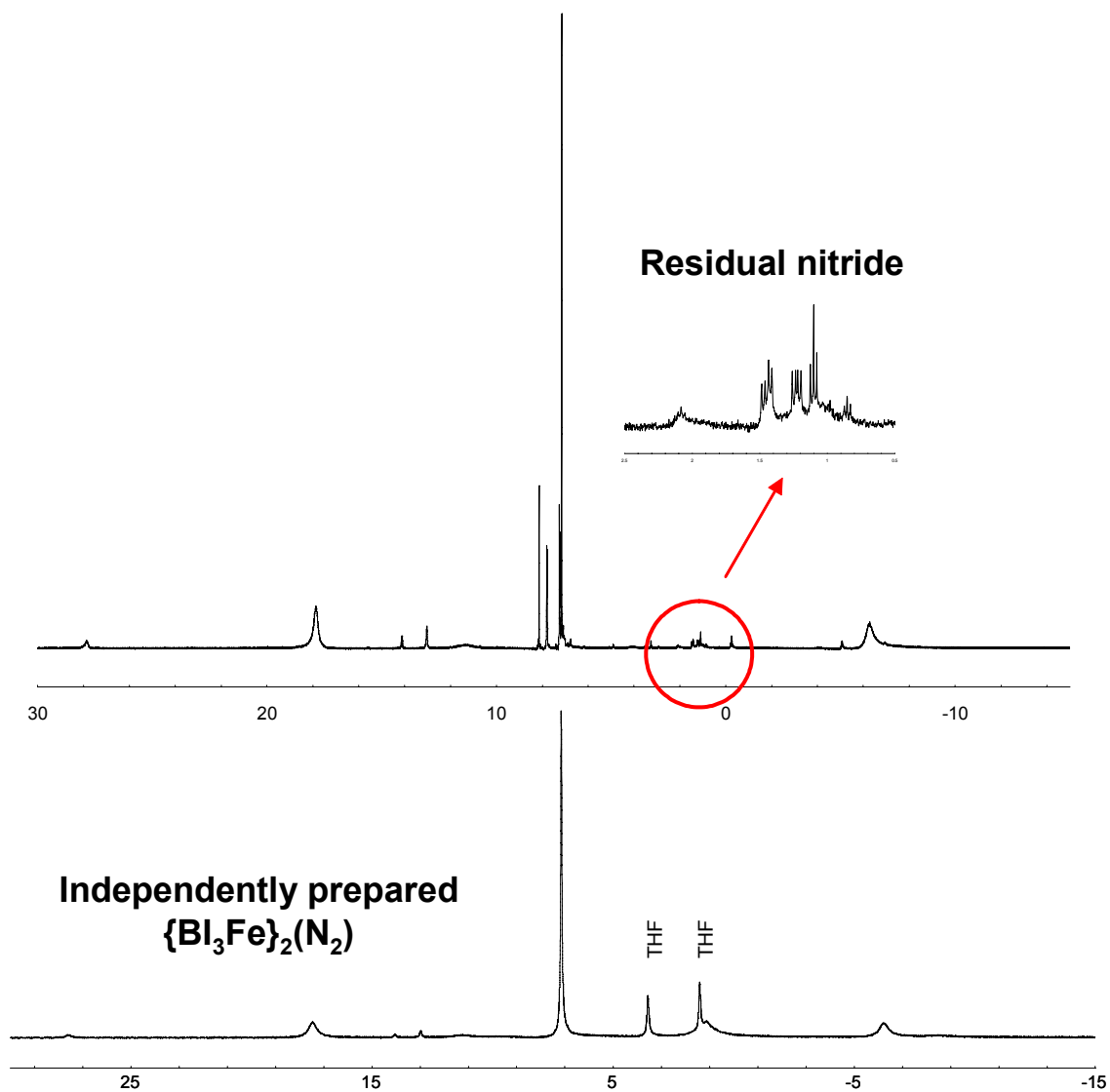
**Figure 4.6.2.** (a, top panel)  $\epsilon$  vs.  $\lambda$  for  $[\text{PhBP}^{i\text{Pr}}_3]\text{Fe}(\text{dbabh})$  decay over time (60 min); (b, lower panel)  $\text{Ln}(\lambda_{475 \text{ time } t} - \lambda_{475 \text{ final}})$  vs. time showing 1<sup>st</sup> order decay of  $[\text{PhBP}^{i\text{Pr}}_3]\text{Fe}(\text{dbabh})$ .



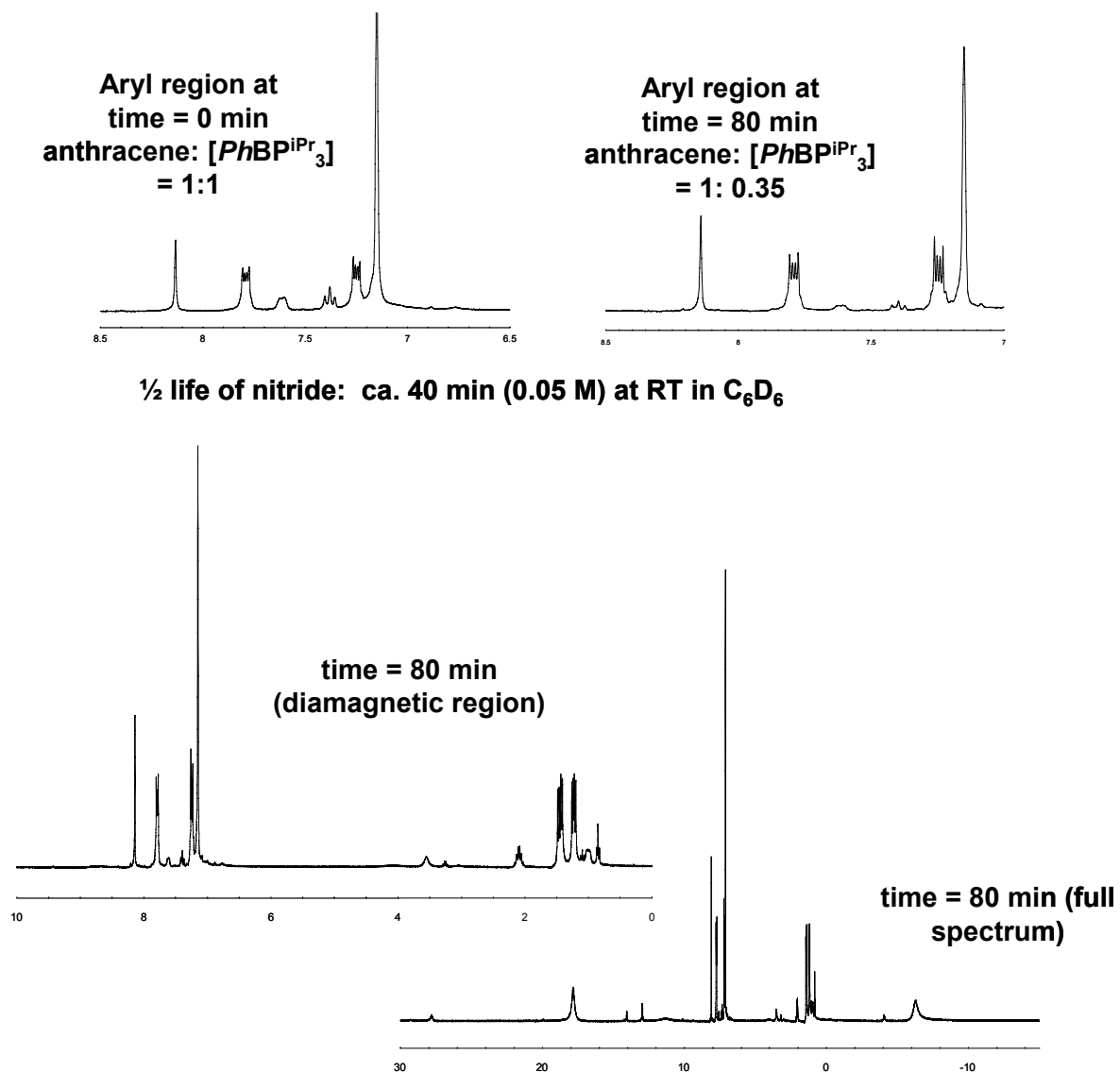
**Nitride coupling experiment in vacuum:** Upon removal of volatiles in vacuum of a 0.05 M solution of  $[\text{PhBP}^{i\text{Pr}}_3]\text{FeN}$  in  $\text{C}_6\text{D}_6$ , the nitride undergoes a bimolecular condensation to produce the monovalent, dinitrogen bridged species  $\{[\text{PhBP}^{i\text{Pr}}_3]\text{Fe}\}_2(\mu\text{-N}_2)$  which has been previously reported.<sup>32</sup> Figure 4.6.3. (top panel) shows the  $^1\text{H}$  NMR ( $\text{C}_6\text{D}_6$ ) obtained from the nitride condensation and the lower panel displays a spectrum ( $^1\text{H}$  NMR ( $\text{C}_6\text{D}_6$ )) of independently synthesized  $\{[\text{PhBP}^{i\text{Pr}}_3]\text{Fe}\}_2(\mu\text{-N}_2)$ . There is also anthracene in the top panel, resulting from the  $[\text{PhBP}^{i\text{Pr}}_3]\text{Fe}(\text{dbabh})$  decomposition reaction.

**Nitride coupling experiment under Ar:** Upon removal of volatiles in vacuum at  $-35\text{ }^\circ\text{C}$  of a 0.05 M solution of  $[\text{PhBP}^{i\text{Pr}}_3]\text{Fe}(\text{dbabh})$  in THF and trituration with pentane at  $-35\text{ }^\circ\text{C}$ , the red solids was transported to an argon box and reconstituted in  $\text{C}_6\text{D}_6$ . The concentration of  $[\text{PhBP}^{i\text{Pr}}_3]\text{FeN}$  was monitored by  $^1\text{H}$  NMR over a period of 8 h. As in the case of the bimolecular condensation of  $[\text{PhBP}^{i\text{Pr}}_3]\text{FeN}$  to produce the dinitrogen bridged species  $\{[\text{PhBP}^{i\text{Pr}}_3]\text{Fe}\}_2(\mu\text{-N}_2)$  under vacuum, 65% of the  $[\text{PhBP}^{i\text{Pr}}_3]\text{FeN}$  has formed the dinitrogen species (see Figure 4.6.4). Figure 4.6.4 (a) shows the aryl region of the  $[\text{PhBP}^{i\text{Pr}}_3]\text{FeN}$   $^1\text{H}$  NMR spectrum at time 0 and  $t = 80$  min. Figure 4.6.4 (b) shows the full spectrum at  $t = 80$  min showing the presence of  $[\text{PhBP}^{i\text{Pr}}_3]\text{FeN}$  and  $\{[\text{PhBP}^{i\text{Pr}}_3]\text{Fe}\}_2(\mu\text{-N}_2)$  as the only two iron-containing species in solution observable by  $^1\text{H}$  NMR.

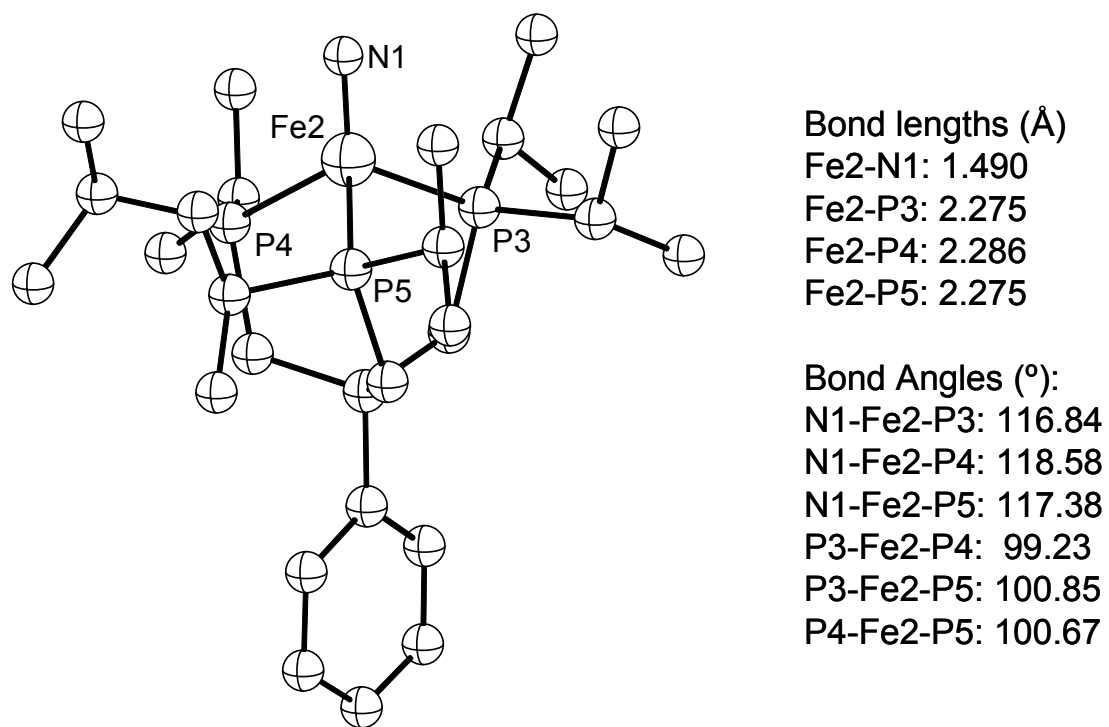
**Figure 4.6.3.**  $^1\text{H}$  NMR of nitride coupling experiment (scales in ppm).



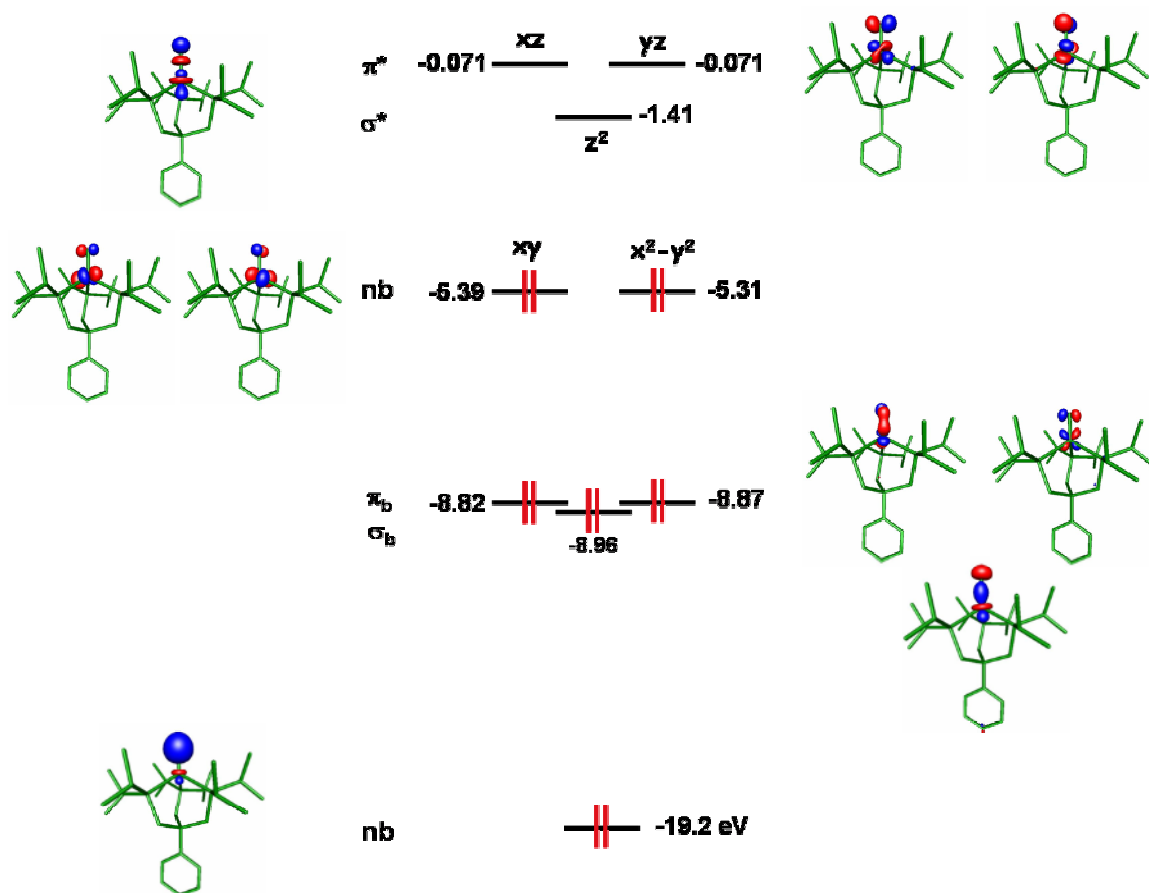
**Figure 4.6.4.**  $^1\text{H}$  NMR of nitride coupling experiment under Argon: (a) aryl region at time = 0 and 80 minutes as indicated; (b) diamagnetic and full  $^1\text{H}$  spectrum of reaction at t = 80 minutes as indicated (scales in ppm).



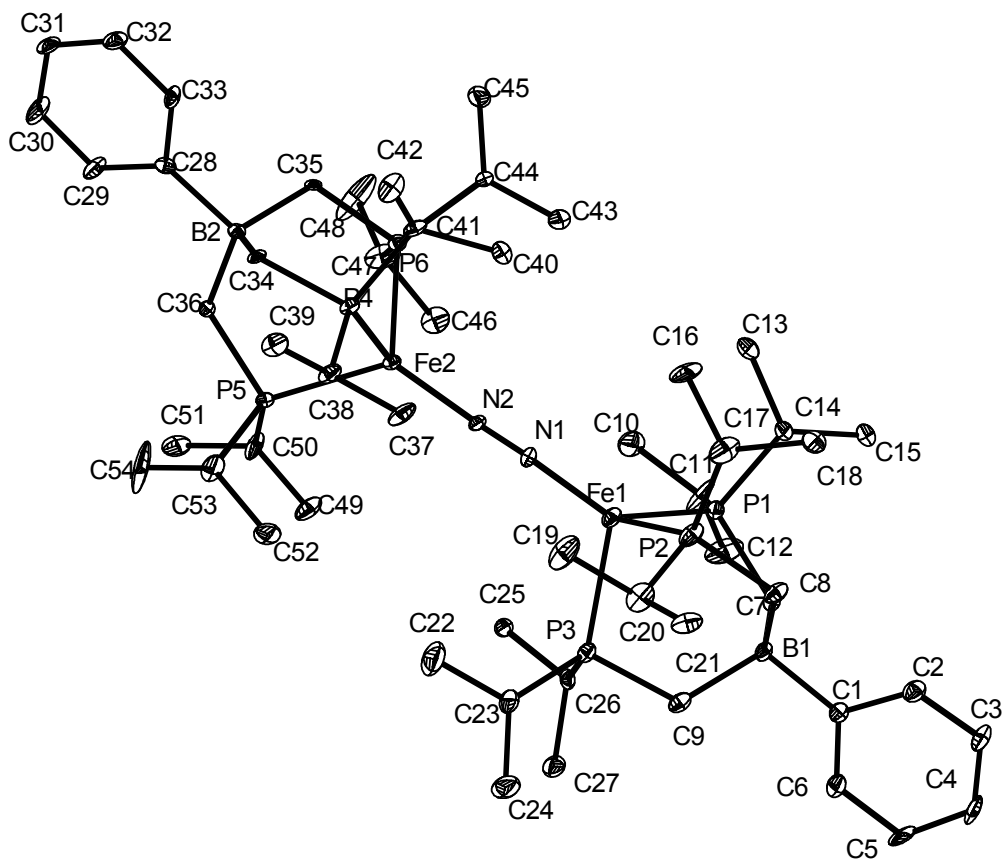
**4.6.6. Electronic Structure Calculations.** A hybrid density functional calculation was performed for  $[\text{PhBP}^{i\text{Pr}}_3]\text{Fe}\equiv\text{N}$  using Jaguar (version 5.0, release 20). The method used B3LYP with LACVP\*\* as the basis set. A geometry optimization was carried out starting from coordinates based on the solid-state structure of  $[\text{PhBP}^{i\text{Pr}}_3]\text{Fe}\equiv\text{NAd}$  (with the adamantyl group removed) that had been determined by an X-ray diffraction study as previously reported as the initial HF guess.<sup>32</sup> No symmetry constraints were imposed and the calculation was performed assuming a singlet electronic state. Figure 4.6.5 shows the geometry/energy minimized structure predicted by Jaguar. Frontier molecular orbitals are displayed in Figure 4.6.6.



**Figure 4.6.5.** DFT predicted structure for  $[\text{PhBP}^{i\text{Pr}}_3]\text{Fe}\equiv\text{N}$ .



**Figure 4.6.6.** Theoretically predicted geometry and electronic structure (DFT, JAGUAR 5.0, B3LYP/LACVP\*\*) for the complex  $[\text{PhBP}^{i\text{Pr}}_3]\text{Fe}\equiv\text{N}$ . A singlet ground state was applied as the only constraint. Lobal representations correspond to the orbitals indicated by the directional arrows.

**Figure 4.6.7.** Displacement ellipsoid (50%) representation of  $\{[\text{PhBP}^{i\text{Pr}}_3]\text{Fe}\}_2(\mu\text{-N}_2)$ .

**Table 4.6.1.** Crystal data and structure refinement for  $\{[\text{PhBP}^{\text{iPr}}_3]\text{Fe}\}_2(\mu\text{-N}_2)$ .

Identification code	tab43	
Empirical formula	$\text{C}_{54}\text{H}_{97}\text{B}_2\text{Fe}_2\text{N}_2\text{P}_6$	
Formula weight	1093.48	
Temperature	100(2) K	
Wavelength	0.71073 Å	
Crystal system	Orthorhombic	
Space group	Pca2(1)	
Unit cell dimensions	$a = 26.3682(17)$ Å	$\alpha = 90^\circ$ .
	$b = 14.3569(9)$ Å	$\beta = 90^\circ$ .
	$c = 32.485(2)$ Å	$\gamma = 90^\circ$ .
Volume	$12297.9(13)$ Å <sup>3</sup>	
Z	8	
Density (calculated)	1.181 Mg/m <sup>3</sup>	
Absorption coefficient	0.662 mm <sup>-1</sup>	
F(000)	4696	
Crystal size	0.185 x 0.185 x 0.3145 mm <sup>3</sup>	
Theta range for data collection	1.25 to 24.84°	
Index ranges	-31 ≤ h ≤ 30, -16 ≤ k ≤ 16, -37 ≤ l ≤ 38	
Reflections collected	96135	
Independent reflections	19520 [R(int) = 0.0622]	
Completeness to theta = 24.84°	95.0 %	
Absorption correction	None	
Refinement method	Full-matrix least-squares on F <sup>2</sup>	
Data / restraints / parameters	19520 / 1 / 1232	
Goodness-of-fit on F <sup>2</sup>	1.645	
Final R indices [I > 2σ(I)]	R1 = 0.0504, wR2 = 0.0973	
R indices (all data)	R1 = 0.0758, wR2 = 0.1019	
Absolute structure parameter	0.603(16)	
Largest diff. peak and hole	0.890 and -0.459 e.Å <sup>-3</sup>	

**Special Refinement Details.** Refinement of F<sup>2</sup> against ALL reflections. The weighted R-factor (wR) and goodness of fit (S) are based on F<sup>2</sup>, conventional R-factors (R) are based on F, with F set to zero for negative F<sup>2</sup>. The threshold expression of F<sup>2</sup> > 2σ(F<sup>2</sup>) is used only for calculating R-factors(gt) etc. and is not relevant to the choice of reflections for refinement. R-factors based on F<sup>2</sup> are statistically about twice as large as those based on F, and R-factors based on ALL data will be even larger.

All esds (except the esd in the dihedral angle between two l.s. planes) are estimated using the full covariance matrix. The cell esds are taken into account individually in the estimation of esds in distances, angles and torsion angles; correlations between esds in cell parameters are only used when they are defined by crystal symmetry. An approximate (isotropic) treatment of cell esds is used for estimating esds involving l.s. planes.

The crystal was twinned and refined as such (BASF = 0.64).

**Table 4.6.2.** Bond lengths [ $\text{\AA}$ ] and angles [ $^\circ$ ] for  $\{[\text{PhBP}^{i\text{Pr}}_3]\text{Fe}\}_2(\mu\text{-N}_2)$ .

---

N(1)-N(2)	1.138(6)
N(1)-Fe(1)	1.811(5)
N(2)-Fe(2)	1.818(5)
Fe(1)-P(3)	2.3395(18)
Fe(1)-P(1)	2.3497(17)
Fe(1)-P(2)	2.3944(18)
N(3)-N(4)	1.211(7)
N(3)-Fe(3)	1.761(7)
N(4)-Fe(4)	1.783(6)
Fe(3)-P(9)	2.3384(16)
Fe(3)-P(8)	2.3403(16)
Fe(3)-P(7)	2.3752(17)
Fe(4)-P(11)	2.3376(17)
Fe(4)-P(12)	2.3709(17)
Fe(4)-P(10)	2.3748(17)
N(2)-N(1)-Fe(1)	173.0(5)
N(1)-N(2)-Fe(2)	171.6(5)
N(1)-Fe(1)-P(3)	112.43(17)
N(1)-Fe(1)-P(1)	112.82(14)
P(3)-Fe(1)-P(1)	97.03(6)
N(1)-Fe(1)-P(2)	136.34(17)
P(3)-Fe(1)-P(2)	93.83(6)
P(1)-Fe(1)-P(2)	96.89(6)
N(2)-Fe(2)-P(4)	105.61(15)
N(2)-Fe(2)-P(6)	125.30(14)
P(4)-Fe(2)-P(6)	96.48(6)
N(2)-Fe(2)-P(5)	129.48(16)
P(4)-Fe(2)-P(5)	95.65(6)
P(6)-Fe(2)-P(5)	96.11(6)
N(4)-N(3)-Fe(3)	173.3(5)
N(3)-N(4)-Fe(4)	172.1(5)
N(3)-Fe(3)-P(9)	114.75(15)
N(3)-Fe(3)-P(8)	110.35(17)
P(9)-Fe(3)-P(8)	96.37(6)
N(3)-Fe(3)-P(7)	136.01(18)
P(9)-Fe(3)-P(7)	96.22(6)
P(8)-Fe(3)-P(7)	95.42(6)
N(4)-Fe(4)-P(11)	108.80(16)
N(4)-Fe(4)-P(12)	120.96(15)
P(11)-Fe(4)-P(12)	96.83(6)
N(4)-Fe(4)-P(10)	131.34(17)
P(11)-Fe(4)-P(10)	94.49(6)
P(12)-Fe(4)-P(10)	96.76(6)

**Figure 4.6.8.** Displacement ellipsoid (50%) representation of  $[\text{PhBP}^{i\text{Pr}}_3]\text{FeNPh}_2$ .

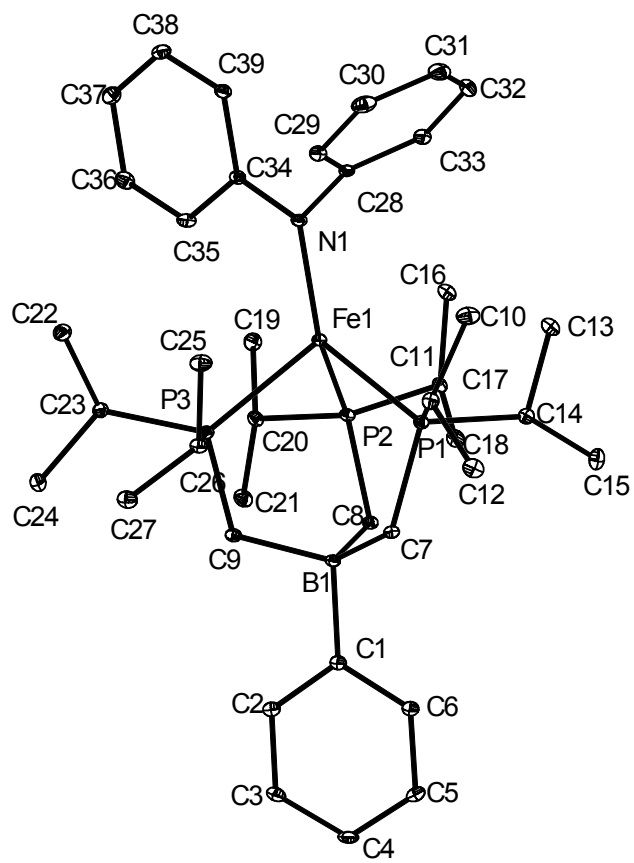


**Table 4.6.3.** Crystal data and structure refinement for [PhBP<sup>iPr</sup><sub>3</sub>]FeNPh<sub>2</sub>.

Identification code	tab47	
Empirical formula	C <sub>39</sub> H <sub>63</sub> BFeNP <sub>3</sub>	
Formula weight	705.47	
Temperature	100(2) K	
Wavelength	0.71073 Å	
Crystal system	Triclinic	
Space group	P-1	
Unit cell dimensions	a = 11.0240(9) Å	α = 87.377(2)°
	b = 13.4574(11) Å	β = 75.6030(10)°
	c = 13.7499(11) Å	γ = 83.956(2)°
Volume	1964.4(3) Å <sup>3</sup>	
Z	2	
Density (calculated)	1.193 Mg/m <sup>3</sup>	
Absorption coefficient	0.533 mm <sup>-1</sup>	
F(000)	760	
Crystal size	0.10 x 0.15 x 0.41 mm <sup>3</sup>	
Theta range for data collection	1.52 to 30.76°	
Index ranges	-15 ≤ h ≤ 15, -18 ≤ k ≤ 19, -19 ≤ l ≤ 19	
Reflections collected	44708	
Independent reflections	11014 [R(int) = 0.0855]	
Completeness to theta = 30.76°	89.9 %	
Absorption correction	None	
Refinement method	Full-matrix least-squares on F <sup>2</sup>	
Data / restraints / parameters	11014 / 0 / 418	
Goodness-of-fit on F <sup>2</sup>	1.273	
Final R indices [I > 2σ(I)]	R1 = 0.0448, wR2 = 0.0797	
R indices (all data)	R1 = 0.0841, wR2 = 0.0906	
Largest diff. peak and hole	0.658 and -0.432 e.Å <sup>-3</sup>	

**Special Refinement Details.** Refinement of F<sup>2</sup> against ALL reflections. The weighted R-factor (wR) and goodness of fit (S) are based on F<sup>2</sup>, conventional R-factors (R) are based on F, with F set to zero for negative F<sup>2</sup>. The threshold expression of F<sup>2</sup> > 2σ(F<sup>2</sup>) is used only for calculating R-factors(gt) etc. and is not relevant to the choice of reflections for refinement. R-factors based on F<sup>2</sup> are statistically about twice as large as those based on F, and R-factors based on ALL data will be even larger.

All esds (except the esd in the dihedral angle between two l.s. planes) are estimated using the full covariance matrix. The cell esds are taken into account individually in the estimation of esds in distances, angles and torsion angles; correlations between esds in cell parameters are only used when they are defined by crystal symmetry. An approximate (isotropic) treatment of cell esds is used for estimating esds involving l.s. planes.

**Table 4.6.4.** Pertinent bond lengths [ $\text{\AA}$ ] and angles [ $^\circ$ ] for  $[\text{PhBP}^{i\text{Pr}}_3]\text{FeNPh}_2$ .

---

Fe(1)-N(1)	1.9527(15)
Fe(1)-P(3)	2.4432(6)
Fe(1)-P(1)	2.4623(6)
Fe(1)-P(2)	2.4669(6)
N(1)-C(34)	1.394(2)
N(1)-C(28)	1.429(2)
N(1)-Fe(1)-P(3)	117.27(5)
N(1)-Fe(1)-P(1)	127.72(5)
N(1)-Fe(1)-P(2)	124.55(5)
P(3)-Fe(1)-P(1)	91.690(19)
P(3)-Fe(1)-P(2)	93.73(2)
P(1)-Fe(1)-P(2)	92.84(2)
C(34)-N(1)-C(28)	115.05(15)
C(34)-N(1)-Fe(1)	125.21(12)
C(28)-N(1)-Fe(1)	119.70(12)
N(1)-C(34)-C(35)	119.56(17)
N(1)-C(34)-C(39)	123.76(17)

**References Cited**

- 
1. (a) Groves, J. T.; Han, Y.-Z. *Cytochrome P450: Structure, Mechanism, and Biochemistry*; Ortiz de Montellano, P. R., Ed.; Plenum Press: New York, 1995; pp 3-48. (b) Costas, M.; Mehn, M. P.; Jensen, M. P.; Que, L., Jr. *Chem. Rev.* **2004**, *104*, 939.
  2. (a) Schlichting, I.; Berendzen, J.; Chu, K.; Stock, A. M.; Maves, S. A.; Benson, D. E.; Sweet, R. M.; Ringe, D.; Petsko, G. A.; Sligar, S. G. *Science* **2000**, *287*, 1615. (b) MacBeth, C. E.; Golombek, A. P.; Young, V. G., Jr.; Yang, C.; Kuczera, K.; Hendrich, M. P.; Borovik, A. S. *Science* **2000**, *289*, 938.
  3. Rohde, J. U.; In, J.-H.; Lim, M. H.; Brennessel, W. W.; Bukowski, M. R.; Stubna, A.; Münck, E.; Nam, W.; Que, L., Jr. *Science* **2003**, *299*, 1037.
  4. (a) Einsle, O.; Tezcan, F. A.; Andrade, S. L. A.; Schmid, B.; Yoshida, M.; Howard, J. B.; Rees, D. C. *Science* **2002**, *297*, 1696. (b) Howard, J. B.; Rees, D. C. *Chem. Rev.* **1996**, *96*, 2965. (c) Burgess, B. K.; Lowe, D. J. *Chem. Rev.* **1996**, *96*, 2983.
  5. (a) Seefeldt, L. C.; Dance, I. G.; Dean, D. R. *Biochemistry* **2004**, *43*, 1401. (b) Chatt, J.; Dilworth, J. R.; Richards, R. L. *Chem. Rev.* **1978**, *78*, 589. (c) Hughes, D. L.; Ibrahim, S. K.; Pickett, C. J.; Querne, G.; Laouenan, A.; Talarmin, J.; Queiros, A.; Fonseca, A. *Polyhedron* **1994**, *13*, 3341. (d) Leigh, G. J. *Science* **2003**, *301*, 55.
  6. Yandulov, D. V.; Schrock, R. R. *Science* **2003**, *301*, 76.
  7. (a) Hills, A.; Hughes, D. L.; Jiminez-Tenorio, M.; Leigh, G. J.; Rowley, A. T. *J. Chem. Soc., Dalton Trans.* **1993**, 3041. (b) George, T. A.; Rose, D. J.; Chang, Y. D.; Chen, Q.; Zubieta, J. *Inorg. Chem.* **1995**, *34*, 1295. (c) Betley, T. A.; Peters, J. C. *J. Am. Chem. Soc.* **2003**, *125*, 10782.

- 
8. (a) Wagner, W. D.; Nakamoto, K. *J. Am. Chem. Soc.* **1988**, *110*, 4044. (b) Meyer, K.; Bill, E.; Mienert, B.; Weyhermuller, T.; Wieghardt, K. *J. Am. Chem. Soc.* **1999**, *121*, 4859.
9. Betley, T. A.; Peters, J. C. *Inorg. Chem.* **2003**, *42*, 5074.
10. Brown, S. D.; Betley, T. A.; Peters, J. C. *J. Am. Chem. Soc.* **2003**, *125*, 322.
11. (a) Carpino, L. A.; Padykula, R. E.; Barr, D. E.; Hall, F. H.; Krause, J. G.; Dufresne, R. F.; Thoman, C. J. *J. Org. Chem.* **1988**, *53*, 2565. (b) Mindiola, D. J.; Cummins, C. C. *Angew. Chem., Int. Ed.* **1998**, *37*, 945.
12. The first-order decay of  $[\text{PhBP}^{\text{iPr}}_3]\text{Fe}(\text{dbabh})$  was established by monitoring the decay of its optical absorption at 475 nm ( $k = 0.067 \text{ M}^{-1} \text{ s}^{-1}$ , 22 °C, 1.2 mM solution; See Experimental Section for details).
13. (a) Laplaza, C. E.; Cummins, C. C. *Science* **1995**, *268*, 861. (b) Yandulov, D. V.; Schrock, R. R. *J. Am. Chem. Soc.* **2002**, *124*, 6252.
14.  $^2J_{\text{PN}}$  coupling is not observed in either the  $^{15}\text{N}$  NMR spectrum or the  $^{31}\text{P}$  NMR spectrum for  $[\text{PhBP}^{\text{iPr}}_3]\text{Fe}\equiv^{15}\text{N}$ . A number of phosphine-supported imides and nitrides that feature other metals (e.g., Mo, W) have been prepared for which  $^{15}\text{N}$  and  $^{31}\text{P}$  NMR data is available.  $^2J_{\text{PN}}$  coupling is not observed in these systems. See: (a) Rocklage, S. M.; Schrock, R. R. *J. Am. Chem. Soc.* **1982**, *104*, 3077. (b) Donovan-Mtunzi, S.; Richards, R. L.; Mason, J. *J. Chem. Soc., Dalton Trans.* **1984**, 1329.
15. (a) Buhr, J. D.; Taube, H. *Inorg. Chem.* **1979**, *18*, 2208. (b) Man, W.-L.; Tang, T.-M.; Wong, T.-W.; Lau, T.-C.; Peng, S.-M.; Wong, W.-T. *J. Am. Chem. Soc.* **2004**, *126*, 478. (c) Seymore, S. B.; Brown, S. N. *Inorg. Chem.* **2002**, *41*, 462.

- 
16. (a) (*trans*-[1,2-Cyclohexanediamino-*N,N'*-bis(4-diethylaminosalicylidene)])Mn<sup>V</sup>≡N was synthesized from *trans*-[1,2-cyclohexanediamino-*N,N'*-bis(4-diethylaminosalicylidene)] according to: Du Bois, J.; Hong, J.; Carreira, E. M.; Day, M. *J. Am. Chem. Soc.* **1996**, *118*, 915. (b) Bendix, J. *J. Am. Chem. Soc.* **2003**, *125*, 13348. (c) Chang, C. J.; Low, D. W.; Gray, H. B. *Inorg. Chem.* **1997**, *36*, 270.
17. For instance, we suspect the reaction solution also contains a bridged nitride species (i.e., Fe=N=Mn). Studies are underway to resolve the complete product profile.
18. [TPP] = tetraphenylporphyrinato; [HIPTN<sub>3</sub>N] = tris(2-(2,4,6,2',4',6'-hexaisopropyl-1,1':3',1''-terphenyl-5'-amino)ethyl)amine.
19. Hill, C. L.; Hollander, F. J. *J. Am. Chem. Soc.* **1982**, *104*, 7318.
20. See Experimental Section for details. *Jaguar*, version 5.0, Schrodinger: Portland, OR, 2002.
21. Jenkins, D. M.; Betley, T. A.; Peters, J. C. *J. Am. Chem. Soc.* **2002**, *124*, 11238.
22. Hay-Motherwell, R. S.; Wilkinson, G.; Hussain-Bates, B.; Hursthouse, M. B. *Polyhedron* **1993**, *12*, 2009.
23. XAS collaboration with Jan-Uwe Rhode and Larry Que, Jr. from University of Minnesota. Data collected at Stanford Linear Accelerator.
24. Lim, M. H.; Rohde, J.-U.; Stubna, A.; Bukowski, M. R.; Costas, M.; Ho, R. Y. N.; Münck, E.; Nam, W.; Que, L., Jr. *Proc. Nat. Acad. Sci.* **2003**, *100*, 3665.
25. Brown, S. D.; Peters, J. C. *J. Am. Chem. Soc.* **2004**, *126*, 4538.
26. While their ground spin-state assignments (EPR, SQUID) are consistent with these formal oxidation states, studies are underway to further probe this family of [PhBP<sup>iPr</sup><sub>3</sub>]Fe-N<sub>x</sub> species by Mössbauer spectroscopy.

- 
27. T. A. Betley, J. C. Peters, *Inorg. Chem.* **42**, 5074 (2003).
28. L. A. Carpino, R. E. Padykula, D. E. Barr, F. H. Hall, J. G. Krause, R. F. Dufresne, C. J. Thoman, *J. Org. Chem.* **53**, 2565 (1988).
29. D. J. Mindiola, C. C. Cummins, *Angew. Chem. Int. Ed.* **37**, 945 (1998).
30. Scarrow, R. C.; Maroney, M. J.; Palmer, S. M.; Que, L., Jr.; Roe, A. L.; Salowe, S. P.; Stubbe, J. *J. Am. Chem. Soc.* **1987**, *109*, 7857.
31. J. Du Bois, J. Hong, E. M. Carreira, M. W. Day, *J. Am. Chem. Soc.* **118**, 915 (1996).
32. T. A. Betley, J. C. Peters, *J. Am. Chem. Soc.* **125**, 10782 (2003).